Title

Analysis of Fault Zone Resonance Modes Recorded by a Dense Seismic Array Across the San Jacinto Fault Zone at Blackburn Saddle

Journal

Journal of Geophysical Research: Solid Earth, 125(10)

ISSN

2169-9313

Authors

Qiu, Hongrui
Allam, Amir A
Lin, Fan-Chi
et al.

Publication Date

2020-10-01

DOI

10.1029/2020jb019756

Peer reviewed

Analysis of Fault Zone Resonance Modes Recorded by a Dense Seismic Array Across the San Jacinto Fault Zone at Blackburn Saddle

Hongrui Qiu[1], Amir A. Allam[2], Fan-Chi Lin[2,3], Yehuda Ben-Zion[4,5]

[1]Department of Earth, Environmental and Planetary Sciences, Rice University, Houston, TX, USA
[2]Department of Geology and Geophysics, The University of Utah, Salt Lake City, UT, USA
[3]Institute of Earth Sciences, Academia Sinica, Taipei, Taiwan
[4]Department of Earth Sciences, University of Southern California, Los Angeles, CA, USA
[5]Southern California Earthquake Center, University of Southern California, Los Angeles, CA, USA

Corresponding author: Hongrui Qiu (hongruiq@rice.edu, qiuhonrui@gmail.com)

Key points:

- Source-independent resonance fault zone wavefield is consistently observed after *S* wave arrival in data recorded by a dense array
- A fault zone model with a low velocity layer between two quarter spaces can fit well the resonance wavefield at ~1.3 Hz
- Modeling the resonance wavefield provides independent constraints on fault zone properties complementary to previous studies

Abstract

We present observations and modeling of spatial eigen-functions of resonating waves within fault zone waveguide, using data recorded on a dense seismic array across the San Jacinto Fault Zone (SJFZ) in southern California. The array consists of 5-Hz geophones that cross the SJFZ with ~10-30 m spacing at the Blackburn Saddle near the Hemet Stepover. Wavefield snapshots after the *S* wave arrival are consistent for more than 50 near-fault events, suggesting that this pattern is controlled by the fault zone structure rather than source properties. Data from example event with high signal to noise ratio shows three main frequency peaks at ~1.3 Hz, ~2.0 Hz, and ~2.8 Hz in the amplitude spectra of resonance waves averaged over stations near the fault. The data are modeled with analytical expressions for eigen-functions of resonance waves in a low-velocity layer (fault zone) between two quarter-spaces. Using a grid search-based method, we investigate the possible width of the waveguide, location within the array, and shear wave velocities of the media that fit well the resonance signal at ~1.3 Hz. The results indicate a ~300 m wide damaged fault zone layer with ~65% *S* wave velocity reduction compared to the host rock. The SW edge of the low-velocity zone is near the mapped fault surface trace, indicating that the damage zone is asymmetrically located at the regionally faster NE crustal block. The imaging resolution of the fault zone structure can be improved by modeling fault zone resonance modes and trapped waves together.

1. Introduction

Fault zones have hierarchical damage structures that include at places core low velocity layers that act as waveguides or trapping structures of seismic waves (e.g. Ben-Zion & Sammis, 2003; Yang, 2015). Some elements of the core fault damage zone can have significant implications for ground motion predictions, properties of earthquake ruptures, and long-term behavior of the fault. As examples, the velocity reduction in the fault zone can lead to considerable amplification of seismic waves (e.g., Spudich & Olsen, 2001; Rovelli et al. 2002; Kurzon et al., 2014), asymmetric damage zones with respect to the fault may be used to infer on preferred propagation direction of earthquake ruptures (e.g. Ben-Zion & Shi, 2005; Dor et al., 2006), and low velocity damage zones can affect properties of earthquake sequences (e.g., Thakur et al., 2020).

The clearest form of fault zone trapped waves (FZTW) are Love-type signals associated with critically reflected phases that interfere constructively within the core damage zone (Ben-Zion & Aki, 1990). These waves follow the *S* body wave with relatively high amplitude and low frequencies, are somewhat dispersive, and they exist predominantly in the vertical and fault parallel components of motion. Love-type trapped waves have been recorded and analyzed at many fault and rupture zones in California (e.g. Catchings et al., 2016; Cochran et al., 2009; Lewis et al., 2005; Li et al., 1990, 1994; Peng et al., 2003; Yang et al., 2011), Japan (e.g. Mamada et al., 2004; Mizuno & Nishigami, 2006), Turkey (e.g. Ben-Zion et al., 2003), Italy (e.g. Avallone et al., 2014; Rovelli et al., 2002), Israel (Haberland et al., 2003) and other locations. A less common type of trapped waves involves leaky modes (normal modes with phase velocities higher than body wave velocities) or Rayleigh-type signals that appear on the radial and vertical components with appreciable amplitudes between the direct *P* and *S* waves (Gulley et al., 2017; Malin et al., 2006). These waves have been observed at the Parkfield section of the San Andreas fault (e.g. Ellsworth & Malin, 2011) and several locations along the San Jacinto fault zone (e.g. Qin et al., 2018; Qiu et al., 2017). Data recorded recently by dense seismic arrays across fault zones enabled also construction of trapped waves from correlations of earthquake waveforms and ambient noise (Hillers et al., 2014; Hillers & Campillo, 2018; Wang et al., 2019).

Normal modes are widely observed on Earth after large earthquakes (e.g. Block et al., 1970) or due to excitation by ocean waves (e.g. Webb, 2008). The energy generated by such sources excites the free oscillations of the earth and produces normal modes (i.e. standing interference pattern) that are only seen at specific eigen-frequencies and can be represented by a set of eigen-functions (e.g. Gilbert, 1971). The observed eigen-frequencies and eigen-functions are sensitive to the earth interior structures and widely used to image the deep earth structures at a global scale (e.g. Dziewonski & Anderson, 1980). Normal modes can be found in any finite object, e.g., freestanding rock arches (Geimer et al., 2020), when energy is trapped inside. Similarly, seismic energy that is trapped in a fault zone waveguide can also produce normal (or resonance) modes within the finite (both in width and depth) waveguide. The corresponding resonance eigen-frequencies and eigen-functions provide constraints on the internal structures of the fault zone waveguide. However, eigen-frequencies and eigen-functions of fault zone resonance waves have never been reported or analyzed so far, likely due to the limitation in seismic station coverage near major faults.

The San Jacinto fault zone (SJFZ) is a major branch of the San Andreas system in southern California and it accommodates a large portion of the plate boundary motion in the region (Fialko, 2006; Lindsey et al., 2014). The SJFZ has significant ongoing seismicity (Hauksson et al., 2012; Ross et al., 2017), and paleoseismic studies show that it is capable of producing large ($M_W > 7.0$) earthquakes (Rockwell et al., 2015, and references therein). To improve the knowledge on local earthquakes and the internal structure of the SJFZ, several seismic arrays were deployed in the last decade across different sections of the fault zone (e.g. Ben-Zion et al., 2015; Li et al., 2019; Wang et al., 2019). Most arrays have relatively short aperture (~500 m) and station spacing of ~50 m. Since typical fault zone width ranges from 100 m to 300 m for the SJFZ (Share et al., 2017, 2019; Qin et al., 2018; Qiu et al., 2017), it is hard to capture with such arrays the energy decay outside and free oscillations inside the fault zone waveguide. However, this may be done with data recorded by a ~2 km long array with instrument spacing of about 10-30 m at the Blackburn Saddle (BS) site of the SJFZ (Fig. 1).

In this study, we aim to investigate the existence and properties of fault zone resonance modes based on the data obtained by the dense array with relatively long aperture at the BS site. By closely examining waveforms for hundreds of regional earthquakes, we are able to robustly observe and confirm for the first time the presence of fault zone resonance modes. Analysis of the natural modal frequencies and eigen-functions in the space-time response of stations spanning the fault zone helps to constrain further properties of the fault zone waveguide, in addition to results based on waveform modeling of FZTW at individual stations. In the following we describe fundamental and first higher fault zone resonance modes observed at stations of the BS array that span the fault zone (Section 3), and develop an analytical-based methodology to infer key geometrical and seismic parameters from the observations (Section 4). The modeling results are presented in section 5 and discussed in section 6. The observations and analyses augment the seismological techniques available for studying fault zone structures.

2. Data & Instrumentation

We deployed a linear array of 108 Fairfield 3C 5-Hz nodal seismometers recording continuously at 1000 Hz sampling rate for 35 days (from 11/21/2015 to 12/26/2015) on the Clark segment of the SJFZ near the Hemet Stepover (Fig. 1a; Allam, 2015). The deployment (BS01-108) was approximately perpendicular (NE to SW) to the fault surface trace in Blackburn Saddle, with station BS55 closest to the mapped fault (Fig. 1b). The array was deployed with station spacing that is ~10 m in a 400 m wide area centered on the mapped fault surface trace and ~30 m elsewhere. The relocated Southern California earthquake catalog of Hauksson et al. (2012, extended to 2018) was used to extract earthquake waveforms (colored star, diamond, and circles in Fig. 1a). Seismic waveforms of ~180 events with magnitude $M > 1.0$ and inside the selected region (blue box in Fig. 1a) are analyzed in this study.

During the analysis, we first remove the mean and linear trend from the seismic waveforms and then apply a bandpass filter of 0.5 and 20 Hz to the data (e.g. Fig. 2). Since Love-type FZTW are polarized primarily in the fault parallel direction (e.g. Ben-Zion & Aki, 1990; Qiu et al., 2017), we rotate the NS and EW components to a coordinate system parallel and perpendicular to the fault strike (AA' in Figs. 1a and 1b). A mean *S* wave pick averaged over the entire array and signal to noise ratio (SNR) are determined automatically for each earthquake using fault parallel component waveforms. The automatic picking algorithm is based on array-mean envelope function (e.g. Baer & Kradolfer, 1987; Fig. S1 and Text S1). Events with SNR smaller than 10 are dropped. The resulting array-mean *S* picks for events near the BS array suggest an average local *S* wave velocity (Vs) of ~2 km/s (red dots in Fig. 3c).

3. Observation of fault zone resonance waves

A low velocity fault zone layer can amplify ground motion at stations near faults by trapping seismic energy (Avallone et al., 2014; Ben-Zion & Aki, 1990). Cormier & Spudich (1984) and Spudich & Olsen (2001) analyzed motion amplification and waveform complexities at fault zone stations in the San Andreas and Calaveras faults in California with ray-tracing and finite-difference calculations. Catchings et al. (2016) used peak ground velocities of fault zone guided waves recorded by cross-fault linear arrays to infer the location and width of the West Napa-Franklin fault zone. Similarly, we find fault-damage-zone related amplification in data recorded by the BS array.

Quantitative analyses of trapped waves were done so far primarily by fitting waveforms, arrival time of phases or dispersion properties of data recorded at one or several stations (e.g. Ben-Zion et al., 2003; Li et al., 1990; Peng et al., 2003; Qiu et al., 2017; Yang et al., 2014). The results provided useful information on the average width, depth, seismic velocity and attenuation coefficient of the trapping structures (e.g. Lewis & Ben-Zion, 2010; Qin et al., 2018; Share et al., 2019). However, significant trade-offs among model parameters limit the imaging resolution based on these analyses and allow only resolving jointly groups of parameters (e.g. Ben-Zion, 1998; Lewis et al., 2005; Jahnke et al., 2002). Different from these FZTW studies, we focus on wavefield snapshots at specific time lapses recorded by the entire array (e.g. upper panel of Animation 1).

Figure 2 shows the bandpass filtered seismic waveforms generated by an example event (Mw 2.98) marked as the yellow star in Fig. 1a. Higher amplitudes and longer durations are observed after the *S* arrival within a narrow zone (~500 m wide; blue solid line in Fig. 2) for both vertical and horizontal components. Figure 3a illustrates the vertical component wavefield of these long-lasting reverberations sampled by the BS array at a specific lapse time, ~3 s after the array-mean *S* pick (e.g. red dashed lines in Fig. 2; “1.52s Relative to Maximum” in Animation 2) for more than 50 near-fault events. The observed pattern of vertical motion across the array is remarkably consistent for all analyzed events over a long period of time after the *S* arrival (Fig. 3a and Animation 2): the amplitude is lowest (~0.2 of the maximum; Fig. 3a) at the edges of the array, i.e. away from the fault zone, and gradually increases towards the central part of the array (from 0 to 500 m; blue bar in Fig. 3a) that agrees well with the section covered by the blue bar shown in Fig. 2.

To demonstrate that such reverberations after *S* waves are also consistently observed at the same group of stations (blue bar in Fig. 3a) for different earthquakes at fault parallel component, we follow Catching et al. (2016) and use peak ground velocities, duration of high amplitudes, and root mean squares of *S* waveforms to identify stations with fault zone resonance waves for each earthquake. Details of the identification process are described in Text S2 and one example is shown in Fig. S2. Figure 3b shows the percentage of events producing detected fault zone resonance waves at each station. Similar snapshots of vertical component wavefield (Fig. 3a) and detections of reverberations with long durations in fault parallel component (Fig. 3b) are observed persistently for different events within the same ~500 m wide zone near the fault surface trace (blue bars in Fig. 3). We interpret this pattern of spatial variability, i.e. amplified motions confined to a narrow zone, and independent of source location and focal mechanism, as controlled by resonance eigen-functions of the local fault damage zone. Since the quality of resonance waves vary significantly for different events, stacking signals over all events may degrade the results. In the subsequent quantitative analysis, we focus on data of the event (yellow star in Fig. 1a) that shows the clearest *S* and resonance wave signals, but find similar results using recordings of other events.

To further model the observed fault zone resonance wavefield, we integrate the fault parallel recordings to displacement seismograms and convolve the resulting waveforms with $1/\sqrt{t}$ for a source conversion, following the processing steps of Ben-Zion *et al.* (2003), Peng *et al.* (2003) and later studies (e.g. Lewis et al., 2005; Qiu et al., 2017). The processed fault parallel component waveforms of the target event (yellow star in Fig. 1a) are shown in Fig. 4a. More pronounced fault zone resonance waves (compared to those shown in Fig. 2b), with long durations and high amplitudes (outlined by the red rectangle), are observed ~1-2 s after the *S* arrival between stations BS29-45. Similar observations are found for recordings of other events (e.g. Fig. S3a). The wave energy is mostly partitioned in the fault parallel direction, as the maximum amplitude of the fault parallel component wavefield outlined by the red box in Fig. 4a is ~2.3 times that of the vertical component, consistent with the polarization analysis shown in Fig. S4. Therefore, in the later analyses, we only focus on the fault parallel component recordings.

Coherent impulsive phases outlined by the black box in Fig. 4a correlate well with the shape of the direct *S* waves, but with much higher amplitudes and a hyperbolic-shape-like arrival pattern across the part of array SW to the Clark fault, likely indicating reflected or converted waves produced by a velocity contrast interface at depth (e.g. Najdahmadi et al., 2016). The strong fault zone reflected or converted waves on the SW side of the fault are consistent with the polarity of the velocity contrast across the fault from regional tomography results (e.g. Allam et al., 2014; Allam & Ben-Zion, 2012) at the BS site. To exclude effects of these impulsive phases, we focus on the resonance wavefield recorded from 25 s to 30 s (black dashed lines in Fig. 4a; hereinafter, the reverberation window).

We use the multitaper spectrum analysis (Prieto et al., 2009) to estimate amplitude spectra (Fig. 4b) of waves in the reverberation window (black dashed lines in Fig. 4a). The dominant frequencies of the mean amplitude spectrum (red curve in Fig. 4c) averaged over stations BS29-45 are around 1.3 Hz, 2.0 Hz, and 2.8 Hz, slightly lower than observations in fault zone trapped wave studies (~5 Hz; e.g. Ben-Zion et al., 2003; Peng et al., 2003; Qiu et al., 2017; Share et al., 2019). Similar set of peak frequencies (~1 Hz, ~2 Hz, and ~3 Hz) are observed in array-mean amplitude spectrum computed for fault zone resonance waves of other events (e.g. Fig. S3b). Note that although ~2 Hz is the strongest peak of the mean amplitude spectrum, the peak frequency of the amplitude spectrum for each station aligns most consistently at the lowest frequency ~1.3 Hz (blue curves in Fig. 4b). Resonance waves at higher modal frequencies (e.g. 2 Hz and 2.8 Hz) are likely more sensitive to the small scale aspects of the fault damage zone, such as a flower-shape variations with depth (e.g. Rockwell & Ben-Zion, 2007; Zigone et al., 2015), and thus generate shifts in peak frequencies between stations within the waveguide. This suggests the solution of a simple fault zone model (Fig. 5) derived in this paper (Section 4.1) is likely to explain observations extracted at 1.3 Hz better than those at higher frequencies. Therefore, we focus on signals filtered at 1.3 Hz in the later analyses and further justify our choice in synthetic tests (Section 4.2).

Figure 6a shows the fault zone resonance wavefield for stations within the 600 m region surrounding the red box depicted in Fig. 4a after narrow bandpass filtering around

1.3 Hz. The filtered waveforms are normalized by the maximum amplitude and arranged with respect to distance from station BS55, closest to the fault surface trace (Share et al., 2019), with positive indicating the NE direction. The wavefield, $V(x,t)$, narrow bandpass filtered at 1.3 Hz ($\omega = 2.6\pi$) can be written as:

$$V(x,t) = |A(x)| \cdot \cos(\omega[t - \tau(x)]), \quad (1)$$

where A and τ denote the amplitude and phase of the wavefield, and x and t indicate the station location (x direction in Fig. 5) and recording time. We first measure the phase delay time, $\tau(x)$, at each station (gray dots in Fig. S5a). The observed phase delay time pattern is not sufficiently smooth, likely due to the noise and coda of the direct *S* wave. Similar effects are observed in the amplitude spatial pattern (gray dots in Fig. S5b). To suppress effects of noise and direct *S* wave coda, we obtain a smoothed fault zone resonance wavefield by first interpolating the phase and amplitude of the raw wavefield (gray dots in Fig. S5) with uniform and finer spatial sampling (5 m spacing; gray curves), and then applying a Savitzky-Golay filter to the interpolated measurements (gray to red curves). Stations with insufficient SNR are excluded. The maximum amplitude of the background wavefield (outside the range from 0 to 600 m) filtered at 1.3 Hz is ~ 17.5% of the maximum; we choose 35% of the maximum of the entire wavefield (gray dashed lines in Figs. 6b and S5b) as the SNR threshold for further analysis. Because of the smoothing, we estimate the uncertainty of the resulting wavefield snapshot at any lapse time as the root mean square of the difference between snapshots extracted from the raw and smoothed fault zone resonance wavefields.

It is interesting to note that the elevation change across the array is 400 m (gray dashed curve in Fig. 7) with the NE side higher than the SW, whereas the phase delay time pattern (red curve in Fig. S5a) shows an opposite trend (i.e. station at higher elevation arrives earlier). If the delay time pattern is due to the topography, the fault damage zone has to dip towards the NE with an angle less than 70º, which is inconsistent with the near-vertical fault zone indicated by both the local and regional imaging results (e.g. Allam & Ben-Zion, 2012; Share et al., 2017, 2019; Zigone et al., 2015). The time delays may be caused by the interference of fundamental and first higher resonance eigen-modes as demonstrated in later synthetic tests (Section 4.2). We assume the fault damage zone is vertical, and correct the topography effect using a reference Vs of 2 km/s (red dots in Fig. 3c). Figure 6b shows the smoothed wavefield after the topographic correction.

The wavefield, $V(x,t)$ in equation 1 can be represented by two snapshots at lapse times τ_0 and $\tau_0 - \frac{\pi}{2\omega}$ ($\omega = 2.6\pi$). Therefore, its complex form (i.e. Hilbert transform) $\hat{V}(x,t)$, is given by

$$\hat{V}(x,t) = \left[V(x,\tau_0) - i \cdot V\left(x, \tau_0 - \frac{\pi}{2\omega}\right)\right] e^{-i\omega(t-\tau_0)}, \quad (2)$$

for any value of τ_0. The solid curves in Fig. 7 illustrate two such wavefield snapshots taken from Fig. 6b at lapse times τ_0 and $\tau_0 - \frac{\pi}{2\omega}$ with τ_0 determined based on a specific criterion described in section 4.2. The shaded areas in Fig. 7 depict estimated uncertainties of the extracted snapshots, which is comparable to the difference between wavefield snapshots using *S* wave velocities of 1.5 km/s and 3 km/s in the topographic correction (dashed curves in Fig. 7). Therefore, instead of modeling the entire resonance wavefield shown in Fig. 6b, we can focus on analyzing the two wavefield snapshots illustrated in Fig. 7.

4. Methodology for mode analysis

4.1 Theoretical background

Ben-Zion & Aki (1990) and Ben-Zion (1998) derived a solution for a wavefield in a structure with vertical fault zone layers excited by an *SH* line source (i.e., a source generating motion parallel to the fault zone layers and the free surface). The general solution for an arbitrary number of vertical layers was applied to a fault zone model with one or two layers between two-quarter spaces, and was widely used to model waveforms of Love-type FZTW recorded by stations inside fault zones (e.g. Avallone et al., 2014; Ben-Zion et al., 2003; Mizuno & Nishigami, 2006; Peng et al., 2003; Qin et al., 2018; Qiu et al., 2017; Share et al., 2017, 2019). Different from the previous FZTW studies, the focus of this paper is to develop an explicit solution for the wavefield of resonance waves (Fig. 4a) observed in section 3 with amplitude decays slowly with time, although propagating inside a fault zone waveguide that is highly attenuative.

For the resonance mode that may exist in a vertical low velocity layer (Fig. 5), the solution for the wavefield satisfying free surface boundary condition, $V(x, z, \omega)$ in frequency domain, associated with the resonance modes is given by (Ben-Zion & Aki, 1990):

$$
\begin{aligned}
V(x \leq 0, z, \omega) &= \int_{-\infty}^{\infty} B_1(k) e^{+\gamma_1 x} \cos(kz)\, dk \\
V(0 \leq x \leq W, z, \omega) &= \int_{-\infty}^{\infty} [B_2^l(k) e^{+\gamma_2 x} + B_2^r(k) e^{-\gamma_2 x}] \cos(kz)\, dk \qquad (3) \\
V(x \geq W, z, \omega) &= \int_{-\infty}^{\infty} B_3(k) e^{-\gamma_3 x} \cos(kz)\, dk,
\end{aligned}
$$

where $k = \omega/c$ is the wavenumber, $\gamma_i = k\sqrt{1 - c^2/\beta_i^2}$ is the horizontal wavenumber in medium *i*, and *x* and *z* are the fault normal and depth coordinates (Fig. 5). ω, *c*, and *W* denote the angular frequency, phase velocity, and fault zone width. β_1, β_2, and β_3 represent the *S* wave velocities in the left quarter space, fault zone, and right quarter space of Fig. 5. Here, the phase velocity *c* satisfies $\beta_2 < c < \min(\beta_1, \beta_3)$. $B_1, B_2^l, B_2^r,$ and B_3 are frequency dependent complex coefficients.

To solve for the *B* coefficients in equation 3, we impose the boundary conditions that displacement and stress are continuous at $x = 0$ and $x = W$ (Ben-Zion & Aki, 1990):

$$
\begin{pmatrix} B_1 \\ 0 \end{pmatrix} = \frac{1}{2I_1} \begin{pmatrix} I_1 + I_2 & I_1 - I_2 \\ I_1 - I_2 & I_1 + I_2 \end{pmatrix} \begin{pmatrix} B_2^l \\ B_2^r \end{pmatrix} \qquad (4a)
$$

$$
\begin{pmatrix} 0 \\ B_3 \end{pmatrix} = \frac{1}{2I_3} \begin{pmatrix} (I_3 + I_2) e^{(\gamma_2 - \gamma_3)W} & (I_3 - I_2) e^{-(\gamma_2 + \gamma_3)W} \\ (I_3 - I_2) e^{(\gamma_2 + \gamma_3)W} & (I_3 + I_2) e^{(\gamma_3 - \gamma_2)W} \end{pmatrix} \begin{pmatrix} B_2^l \\ B_2^r \end{pmatrix}, \qquad (4b)
$$

where $I_i = \mu_i \gamma_i$ and μ_i are the impedance and shear moduli of medium *i*. By solving equations 4a and 4b, we get the following relations:

$$
\begin{aligned}
B_1 &= \frac{2I_2}{I_1 + I_2} B_2^l \\
B_2^r &= \frac{I_2 - I_1}{I_1 + I_2} B_2^l \\
B_3 &= \left(e^{(\gamma_2 + \gamma_3)W} + \frac{I_2 - I_1}{I_1 + I_2} e^{(\gamma_3 - \gamma_2)W} \right) B_2^l \qquad (5) \\
e^{-2\gamma_2 W} &= \frac{(I_1 + I_2)(I_3 + I_2)}{(I_1 - I_2)(I_3 - I_2)}.
\end{aligned}
$$

The last relation in the equation set 4 is the transcendental dispersion equation (Ben-Zion & Aki, 1990). Since γ_2 and I_2 are complex values, we can rewrite the dispersion relation as:

$$\tan\left[W\omega\sqrt{\beta_2^{-2}-c^{-2}}\right] = \frac{\mu_2\sqrt{\beta_2^{-2}-c^{-2}}\cdot\left(\mu_1\sqrt{c^{-2}-\beta_1^{-2}}+\mu_3\sqrt{c^{-2}-\beta_3^{-2}}\right)}{\mu_2^2(\beta_2^{-2}-c^{-2})-\mu_1\mu_3\sqrt{(c^{-2}-\beta_1^{-2})\cdot(c^{-2}-\beta_3^{-2})}}, \tag{6}$$

The solution of equation 6 indicates a finite number (e.g. 3 crossings in Fig. 8a) of allowable phase velocities, c_j, for a given fault zone model (Fig. 5) and angular frequency ω. Let $B_{2\_j}^l$ be the B_2^l for the *j*-th eigen-mode; we then can rewrite equation 3 as:

$$V(x, z=0, \omega) = \sum_{j=0}^{n-1} B_{2\_j}^l \cdot u_j(x,\omega), \tag{7a}$$

where *j* and *n* are the index and total number of all allowable phase velocities that satisfy the dispersion equation 6. We set $z = 0$ assuming the seismic stations are deployed on a flat surface. $u_j(x,\omega)$ is the eigen-function at angular frequency ω for the *j*-th mode:

$$\begin{aligned} u_j(x\le 0,\omega) &= \frac{2I_2}{I_1+I_2}e^{\gamma_1 x} \\ u_j(0\le x\le W,\omega) &= e^{\gamma_2 x}+\frac{I_2-I_1}{I_1+I_2}e^{-\gamma_2 x} \\ u_j(x\ge W,\omega) &= \left(e^{\gamma_2 W}+\frac{I_2-I_1}{I_1+I_2}e^{-\gamma_2 W}\right)\cdot e^{-\gamma_3(x-W)}, \end{aligned} \tag{7b}$$

whereas in time domain, $u_j(x,t)$ can be expressed as $\hat{u}_j(x)e^{-i\omega(t-t_0)}$. Since $\gamma_2 = i\overline{\gamma_2}$ is a complex value ($\overline{\gamma_2} = \omega\sqrt{\beta_2^{-2}-c^{-2}}$ is a real coefficient), equation 7b indicates that the eigen-functions of the resonance wave are characterized by a sinusoidal function inside the fault zone layer, and an exponential decay outside.

Based on equation 5, we can solve all the coefficients as expressions of $B_{2\_j}^l$. Thus, the shapes of single mode eigen-functions (eq. 7b) are independent of $B_{2\_j}^l$, but the total displacement wavefield of the resonance wave, *V*, can vary depending on the different combination of mode coefficients $B_{2\_j}^l$ (eq. 7a). Although we cannot solve $B_{2\_j}^l$, the ratio $R_j = B_{2\_j}^l / B_{2\_0}^l$ can be determined (Text S3) using the location (x_s, z_s) where energy enters the fault damage zone (Fig. 5; hereinafter, the perturbation source location). It is interesting to note that the depth of the source z_s only affects the phase of the complex coefficient R_j, whereas the lateral source location x_s can alter both the phase and amplitude (Text S3). Since the above equations are derived in the frequency domain, we convert the total wavefield (eq. 7a) to time domain:

$$V(x,t;\omega) = \mathrm{real}\left[e^{-i\omega t} \cdot B_0(\omega) \sum_{j=0}^{n-1} R_j \cdot u_j(x,\omega)\right], \tag{8}$$

where B_0 is a frequency dependent constant. Since R_j is a complex coefficient, meaning different resonance eigen-modes can oscillate with a different initial phase, the total wavefield $V(x,t;\omega)$ may yield more complex pattern (e.g. Fig. 6) than that of a single resonance mode (eq. 7b) when two or more resonance eigen-modes are present.

The solution for the fault zone model depicted in Fig. 5 does not provide constraints on the resonance (or natural) frequencies. The frequency dependent constant B_0 (eq. 8) cannot be resolved from the equations derived in this section, likely due to the limitation that the depth of the assumed fault zone layer is infinite. We therefore are not able to explain the three dominant frequency peaks (~1 Hz, ~2 Hz, and ~3 Hz) in the average amplitude spectrum of the resonance waves recorded at the BS array (Figs. 4c and S4b).

In summary, for a set of given fault zone parameters (Fig. 5), we can first solve the number and phase velocities of all allowable resonance eigen-modes through the dispersion equation 6 for a certain frequency. Then, the analytical formation of each eigen-mode as a function of sensor location on the surface can be derived (starting from the fundamental mode) using equation 7. To generate a synthetic wavefield corresponding to resonance modes recorded by a dense linear array crossing a fault zone waveguide, the contribution of each eigen-mode and the resulting wavefield are given by R_j (Text S3) and equation 8.

4.2 *Synthetic results*

The data of the BS array were used previously for analyses of fault zone head and trapped waves (Share et al., 2019) and surface waves dispersion curves (Li et al., 2019) recorded by some stations. The results from these studies indicated that the Clark fault surface trace at BS (AA' in Fig. 1b) separates two distinctive crustal blocks with the SW having slower seismic velocities, and the existence of a low velocity damage zone on the NE of the fault. Share et al. (2019) found fault zone head waves traveling both along a deep bimaterial fault interface and also along a local velocity contrast at the edge of the damage zone. Results associated with the deep biomaterial interface revealed ~10% contrast in *P* wave velocities to the SE from the array, with the crustal block on the NE side of the fault being faster. However, the velocity contrast likely decreases to ~3% near the BS site (Share et al., 2017). Teleseismic delay time analysis indicated a low velocity zone that is ~270 m wide, while trapped wave modeling results imaged a narrower core damage zone (~150 m) with ~55% reduction in shear velocity extending to ~2 km depth. Li et al. (2019) investigated the recorded ambient noise data and constructed a detailed 2-D Vs model for fault zone structures at BS in the top 1 km. By incorporating topography in the analysis, Li et al. (2019) imaged a low velocity zone that is narrowing with depth in the top 500 m, with the main damage zone (~400 m wide) NE of the mapped surface trace of the Clark fault.

To illustrate the equations derived in section 4.1, we assume the velocity contrast is the same for *P* and *S* waves at the BS site. We use a fault zone model (Fig. 5) that has $\beta_2/\beta_1 = 0.45$ and $\beta_3/\beta_1 = 1.03$ following the results of Share et al. (2019), and $\beta_1 = 2$ km/s (mean Vs of red circles in Fig. 3c) to compute synthetic resonance wavefield at 3 Hz (the highest peak frequency of Figs. 4c and S3b). We set the density to a constant value of 2.7×10^3 kg/m^3 in the subsequent analyses, as changes in density have negligible effect on the synthetic results. We use a fault zone width of 400 m (Li et al., 2019) to show a case that yields three resonance eigen-modes (u_j in eq. 7) with different phase velocities. The contribution of each eigen-mode, ratio R_j (eq. 8), is calculated using $x_s = 0$ m and $z_s = 1.5$ km.

Figure 8a shows numerical solutions (crossings in red) of three phase velocities, and the total resonance wavefield in time domain is illustrated in Fig. 8b. As indicated by equation 6 and Fig. 8a, the number of phase velocity solutions depends on the range of $X = W\omega\sqrt{\beta_2^{-2} - c^{-2}} = W\overline{\gamma_2}$, the *x*-axis of Fig. 8a, i.e. a wider range likely has more solutions. Let $\beta_{\min} = \min(\beta_1, \beta_3)$; the range of *X*, given by $\left(0, \frac{W\omega}{\beta_{\min}}\sqrt{\left(\frac{\beta_{\min}}{\beta_2}\right)^2 - 1}\right)$, increases with the angular frequency and width (ω and *W*) but decreases with $\beta_2/\beta_{\min}$ (<

1) and $\beta_{\min}$. This relation indicates that a model can generate more and higher resonance modes for waves at shorter wavelength or in a wider fault zone layer with more damage. The location of the perturbation source (x_s = 0) and the 3% Vs contrast ($\beta_3/\beta_1 = 1.03$) are responsible for the observed asymmetry with respect to the fault zone center (x = 200 m) in the total resonance wavefield (Fig. 8b). This is demonstrated by the symmetric wavefield (Fig. S6) obtained by changing the perturbation source to the fault zone center (x_s = 200 m) and set $\beta_3/\beta_1 = 1$.

Fig. 9 illustrates the snapshots and relative phase patterns of the eigen-functions (solved in the frequency domain using eq. 7b) and the total resonance wavefield. The number of zero crossings marks the degree of eigen-mode (e.g. 0, 1, and 2 zero crossings for the fundamental, first higher, and second higher modes in Fig. 9). This is because the distance between two nearby phase velocity solutions (or zero crossings) in Fig. 8a, given by $W \cdot [\overline{\gamma_2}(c_{i+1}) - \overline{\gamma_2}(c_i)]$ in equation 6, is approximately equal to π (one period of tangent function). Using approximation in equation 7b suggests that the eigen-function of the $i+1$-th mode, which is characterized by a sinusoidal function within the fault zone layer, has about half cycle of oscillations (and thus one zero crossing) more than that of the i-th mode.

We also compute theoretical resonance eigen-modes for the same fault zone model at 1.3 Hz (Fig. S7). The number of resonance eigen-modes is larger at 2.0 Hz and 2.8 Hz. This is demonstrated in both synthetic calculations, i.e. three modes at 3 Hz (Fig. 8a) but only one mode at 1.3 Hz (Fig. S7a), and observations at the BS array, i.e. wavefield of resonance waves at higher frequency show more zero crossings (Animations 3-5). Therefore, the modeling results of observations at 2.0 Hz and 2.8 Hz are likely subjected to stronger trade-offs between model parameters. This is because the number of independent wavefield snapshots extracted from observations (eq. 2) is the same for all frequencies, but more resonance modes exist at higher frequency, making the modeling process less determined. We thus focus on modeling the resonance wavefield only at the lowest peak frequency 1.3 Hz (Fig. 4c).

The total resonance wavefield yields complicated spatial patterns (Fig. 8b) and relative phase (top curves in Fig. 9). Figure 10 demonstrates the dependence between the total resonance wavefield and the complex coefficients $R_j = B^l_{2\_j}/B^l_{2\_0}$, the contribution of the j-th eigen-modes. Although the variation in R_j can alter the resulting wavefield significantly, the shape of eigen-modes for the fault zone resonance is preserved. Thus, instead of analyzing the total resonance wavefield, we focus on fitting the two snapshots at lapse times τ_0 and $\tau_0 - \frac{\pi}{2\omega}$ following equation 2. Since a maximum number of one zero crossing is found in the wavefield filtered at 1.3 Hz (Fig. 6 and Animation 1), no second or higher modes exist in the observed resonance waves at 1.3 Hz, i.e. consisting of only the fundamental and first higher eigen-modes. Thus, we can further simplify the modeling of resonance waves by choosing τ_0 that satisfies

$$\rho(\tau_0; \omega) = \min_t[\rho(t; \omega)] = 0, \tag{9a}$$

where $\rho(t)$ is given by (e.g. black curve in Fig. 10)

$$\rho(t; \omega) = \text{abs}\left\{\min_x[V(x, t; \omega)] + \max_x[V(x, t; \omega)]\right\}. \tag{9b}$$

Determination of such lapse times τ_0 and $\tau_0 - \frac{\pi}{2\omega}$ is shown in Fig. 10 with red and green dashed lines. The corresponding wavefield snapshots at these two lapse times are shown in Fig. 11. As illustrated in equation 7b, the eigen-function of a resonance mode is represented by a sinusoidal function within fault zone. Therefore, $\rho(t)$ is always positive when the fundamental mode (no zero crossing; e.g. Fig. 9a) is present. This is supported by the observation in Fig. 11 that the snapshot at lapse time τ_0 (in red) overlaps with the first higher mode eigen-function (black dashed curves) after self-normalization, suggesting oscillation of the fundamental mode becomes zero when $\rho(t)$ is zero. Thus, since only two modes are present in the wavefield of resonance waves at 1.3 Hz ($\omega = 2.6\pi$), we first extract and model the wavefield snapshot at $t = \tau_0$ (red dashed line in Fig. 6b), $V(x, \tau_0)$, as the eigen-function of the first higher resonance mode (red curve in Fig. 7). Then, the wavefield snapshot at $t = \tau_0 - \frac{\pi}{2\omega}$ (black dashed line in Fig. 6b), $V\left(x, \tau_0 - \frac{\pi}{2\omega}\right)$, that contains information of the fundamental mode (black curve in Fig. 7) can also contribute to misfit calculation for the modeling of resonance waves.

4.3 Inversion for waveguide parameters

In section 4.1, we derived the formation of eigen-functions for resonance waves in a fault zone model shown in Fig. 5. Furthermore, we demonstrated in section 4.2 that the narrow bandpass filtered resonance wavefield can be represented by wavefield snapshots extracted at two specific lapse times (τ_0 and $\tau_0 - \frac{\pi}{2\omega}$; eq. 2), and the snapshot at τ_0 for 1.3 Hz corresponds to the first higher mode eigen-function. Here we utilize the grid search method to find fault zone parameters that can explain the resonance wavefield at the lowest peak frequency (Animation 1; Fig. 6b), or equivalent to, $V\left(x, \tau_0 - \frac{\pi}{2\omega}\right)$ and $V(x, \tau_0)$, wavefield snapshots for 1.3 Hz extracted at lapse times $\tau_0 - \frac{\pi}{2\omega}$ and τ_0 (solid curves in Fig. 7), within the estimated uncertainty (shaded areas in Fig. 7).

As the spatial distribution of the eigen-mode is independent to the perturbation source location (x_s and z_s in Fig. 5), we only include the fault zone width, *W*, and *S*-wave velocities, β_1, β_2, and β_3, in the inversion (Fig. 5). For each fault zone model, we first calculate the eigen-functions for the fundamental and first higher resonance modes at 1.3 Hz ($\omega = 2.6\pi$), $\hat{u}_0(x)$ and $\hat{u}_1(x)$, using equation 7b. We then determine x_c, center location of the fault zone, by minimizing

$$\delta_1(x_c) = \sum_x [\tilde{V}(x, \tau_0) - \tilde{u}_1(x')]^2, \tag{10a}$$

where $x' = x + x_c - \frac{W}{2}$. $\tilde{V}$ and $\tilde{u}$ indicate the self-normalized V and $\hat{u}$, respectively. To further fit $\tilde{V}\left(x, \tau_0 - \frac{\pi}{2\omega}\right)$, self-normalized wavefield snapshot at lapse time $\tau_0 - \frac{\pi}{2\omega}$ that is a summation of both resonance eigen-modes, we grid search a coefficient, $-1 \leq \alpha \leq 1$, that minimizes

$$\delta_2(\alpha) = \sum_x \left\{\tilde{V}\left(x, \tau_0 - \frac{\pi}{2\omega}\right) - [\tilde{u}_0(x') + \alpha \cdot \tilde{u}_1(x')]/\xi\right\}^2, \tag{10b}$$

where $\xi = \max_{x'}[\tilde{u}_0(x') + \alpha \cdot \tilde{u}_1(x')]$. We note that α is sensitive to the ratio R_1/R_0 (eq. 8) and thus the perturbation source location (Text S3) and set $|\alpha| \leq 1$ as $\tilde{V}\left(x, \tau_0 - \frac{\pi}{2\omega}\right) > 0$ for all x within fault zone (black curve in Fig. 7). In the case of modeling the two wavefield snapshots, $V\left(x, \tau_0 - \frac{\pi}{2\omega}\right)$ and $V(x, \tau_0)$, individually, i.e. assuming $V\left(x, \tau_0 - \frac{\pi}{2\omega}\right)$ is representative of the fundamental eigen-mode that is produced by a set of model parameters different from that of the first higher eigen-mode $V(x, \tau_0)$, we just set $\alpha = 0$ in equation 10b.

The data misfit for wavefield snapshots at lapse time τ_0 is defined as

$$\chi^2(W,\beta_1,\beta_2,\beta_3;\tau_0) = \min[\delta_1(x_c)]/[\sigma(\tau_0)\cdot N_x] \quad (11a)$$

and at lapse time $\tau_0 - \frac{\pi}{2\omega}$ as

$$\chi^2\left(W,\beta_1,\beta_2,\beta_3;\tau_0 - \frac{\pi}{2\omega}\right) = \min[\delta_2(\alpha)]/\left[\sigma\left(\tau_0 - \frac{\pi}{2\omega}\right)\cdot N_x\right], \quad (11b)$$

where N_x is the number of data points and σ indicates the estimated uncertainty (shaded areas in Fig. 7). When fitting both wavefield snapshots with the same set of model parameters, the overall misfit value is defined as

$$\bar{\chi}^2(W,\beta_1,\beta_2,\beta_3) = \left[\chi^2(W,\beta_1,\beta_2,\beta_3;\tau_0) + \chi^2\left(W,\beta_1,\beta_2,\beta_3;\tau_0 - \frac{\pi}{2\omega}\right)\right]/2 \quad (11c)$$

5. Results

5.1 Fault Zone Resonance at 1.3 Hz

Figure 6b shows the resonance wavefield at 1.3 Hz after smoothing and topographic correction, and Fig. 7 illustrates the two snapshots that are taken at time lapses determined following equation 9 (Section 4.2). In general, the smoothed wavefield snapshot for 1.3 Hz observed at $t = \tau_0$ (red curve in Fig. 7), $V(x,\tau_0)$, shows consistent features as observed in the synthetic first higher eigen-mode (e.g. Figs. 9 and 11; sinusoidal function with one zero crossing inside the fault zone layer). We noticed that $V(x,\tau_0)$ is asymmetric (red curve in Fig. 7) with amplitude decay slightly faster towards the SW (negative *x*) relative to the NE (positive *x*). There are several potential mechanisms for the observed asymmetry, such as $\beta_1 \neq \beta_3$ (velocity contrast across fault), residual topographic effect (Vs ≠ 2 km/s at the BS site), and lack of attenuation in the derivation. Similar asymmetry has been observed for $V\left(x,\tau_0 - \frac{\pi}{2\omega}\right)$, the smoothed wavefield snapshot for 1.3 Hz at $t = \tau_0 - \frac{\pi}{2\omega}$ (black curve in Fig. 11), which could also be related to the fact that it is a summation of two (the fundamental and first higher) eigen-modes.

5.2 Modeling of Eigen-functions

Here we model the two wavefield snapshots shown in Fig. 7, equivalent to the wavefield resonating at 1.3 Hz within the fault zone (Fig. 6b), based on the simplified fault zone model shown in Fig. 5. We first discretize the parameter space as follows: (a) fault zone width *W* from 100 m to 500 m with 20 m increment; (b) β_1 from 0.5 km/s to 4.5 km/s with 0.2 km/s as the interval; (c) β_2/β_1 from 0.1 to 0.9 with a step of 0.02; (d) β_3/β_1 from 0.6 to 1.4 with a step of 0.05. In total, 307377 models are examined. For each fault zone model, we calculate the χ^2 misfit for wavefield snapshots at τ_0, i.e. $\chi^2(\tau_0)$, and $\tau_0 - \frac{\pi}{2\omega}$, i.e. $\chi^2\left(\tau_0 - \frac{\pi}{2\omega}\right)$, and compute the overall $\bar{\chi}^2$ misfit following equation 11.

Figure 12 shows the resulting histograms for all three metrics of misfit (eq. 11). The number of models with misfit value less than 13 is much larger for $\chi^2\left(\tau_0 - \frac{\pi}{2\omega}\right)$ (Fig. 12c). This is because we do not exclude fault zone models that generate merely the fundamental resonance mode and only calculate the misfit $\chi^2\left(\tau_0 - \frac{\pi}{2\omega}\right)$ for these models. The minimum misfit value of $\chi^2(\tau_0)$ is smaller than that of $\chi^2\left(\tau_0 - \frac{\pi}{2\omega}\right)$, suggesting that the wavefield snapshot at τ_0 is better fitted than at $\tau_0 - \frac{\pi}{2\omega}$. This is consistent with the results shown in Figs. 13a and 13b, where model predicted wavefield snapshots (gray curves) at τ_0 and $\tau_0 - \frac{\pi}{2\omega}$ with $\bar{\chi}^2$ misfit values less than 1.5 times the minimum (0.96; top right of Fig. 13b) are depicted on top of the observed patterns (blue curve). Synthetic wavefield snapshots of the selected models fit well the observed pattern within the estimated uncertainty range (blue dashed curves) at τ_0 (Fig. 13a) but not at $\tau_0 - \frac{\pi}{2\omega}$ (Fig. 13b). As there is a group of fault zone models with misfit values close to the minimum, instead of focusing on the best fitting fault zone parameters (bottom left of Fig. 13b) it is more reliable to investigate the group of model parameters (Fig. 14) that fit the data within the estimated uncertainty.

There are three different misfit metrics calculated for each fault zone model (eq. 11), so one can determine model parameters based on these three metrics separately. Figures 13a, 13b, and 14 demonstrate results associated with $\bar{\chi}^2$ misfit. The selection of models based on $\bar{\chi}^2$ misfit aims to fit both wavefield snapshots simultaneously with the same fault zone model. Similarly, we show the theoretical wavefield snapshots computed using fault zone parameters selected based on misfits defined by equations 11a and 11b, $\chi^2(\tau_0)$

and $\chi^2\left(\tau_0 - \frac{\pi}{2\omega}\right)$, in Figs. 13c and 13d, respectively. The corresponding groups of model parameters that yield a misfit value less than 1.5 times the minimum are illustrated in Figs. 15 and S8. The model parameters selected based on $\chi^2(\tau_0)$ and $\chi^2\left(\tau_0 - \frac{\pi}{2\omega}\right)$ are optimized to fit the observed wavefield snapshot at τ_0 and $\tau_0 - \frac{\pi}{2\omega}$, respectively.

Based on models selected using $\bar{\chi}^2$ misfit (Figs. 13a, 13b, and 14), the best fitting fault zone model is 280 m wide with ~ 40% Vs reduction compared to the surrounding host rock. However, the inferred Vs of the host rock is less than 1 km/s, which is much lower than that indicated by the direct *S* arrivals (~2 km/s; Fig. 3c). Instead of adopting the best fitting model parameters, we compute the weighted average value of fault zone parameters over all selected models (green dots in Fig. 14) to account for the uncertainty of the observations and trade-offs between parameters (using fault zone width as an example):

$$\bar{W} = \sum(W/\bar{\chi}^2)\Big/\sum(1/\bar{\chi}^2)\,. \qquad (12)$$

The weighted average model parameters are fault zone width of 320 m and Vs reduction of 65%, with 2 km/s Vs of the surrounding host rock, which are comparable to the values inferred by Share et al. (2017). We note that β_3/β_1 is fixed as 1 in the FZTW modeling of Share et al. (2017) and (2019). The β_3/β_1 values for the selected models are mostly less than 1, suggesting locally faster Vs on the SW side than the NE. This is in contrast to the regional velocity contrast inferred from tomography (e.g. Allam & Ben-Zion, 2012). The local reversal of the velocity contrast with respect to the regional contrast is produced by the damaged fault zone structure.

The minimum misfit values of $\chi^2(\tau_0)$, 0.3 (Fig. 13c), and $\chi^2\left(\tau_0 - \frac{\pi}{2\omega}\right)$, 0.63 (Fig. 13d), are much smaller than that of $\bar{\chi}^2$ (0.96; Fig. 13b). Moreover, the fault zone models selected based on $\chi^2\left(\tau_0 - \frac{\pi}{2\omega}\right)$ (gray curves in Fig. 13d) can only generate the fundamental resonance mode. These observations suggest that the wavefield snapshots measured at two different lapse times, equivalent to the fundamental (snapshot at $\tau_0 - \frac{\pi}{2\omega}$; black curve in Fig. 11) and first higher (snapshot at τ_0; red curve in Fig. 11) eigen-modes, are likely produced by two resonance structures with very different parameters (e.g. width and velocity). The average parameters of models selected based on $\chi^2(\tau_0)$ indicate a fault zone with ~360 m wide and ~64% Vs reduction (Fig. 15), whereas the values for $\chi^2\left(\tau_0 - \frac{\pi}{2\omega}\right)$ are ~170 m and ~30% (Fig. S8). Consistent with results inferred from misfit $\bar{\chi}^2$, β_3/β_1 of models selected based on $\chi^2(\tau_0)$ (~0.8; Fig. 15d) also indicate a reversal of what is found in previous studies at BS ($\beta_3/\beta_1 > 1$; e.g. Fig. 13 of Share *et al.* 2017). For results associated with the misfit $\chi^2\left(\tau_0 - \frac{\pi}{2\omega}\right)$, the same reversal in β_3/β_1 (< 1) is observed, but the contrast $(1 - \beta_3/\beta_1)$ is much smaller (~6%; Fig. S8d) compared to that of $\chi^2(\tau_0)$ (~20%; Fig. 15d). This local reversal and large Vs contrast across the fault are likely associated with a transition zone in the NE, as the region with fault related rock damage is broader than the localized fault zone waveguide and located asymmetrically within the faster NE crustal block (Share et al., 2019). Similar reversals in the sense of velocity contrast across the fault (β_3/β_1) resolved at the local scale (< 1 km) with respect to that of the regional scale (a few kilometers) were observed in other sections of the SJFZ (Lewis et al., 2005; Qiu et al., 2017; Qin et al., 2018).

6. Discussion

We develop and implement an analytical framework to explain long duration resonance waves observed after FZTW at the BS site of the SJFZ (Figs. 1-3). A reasonably good data fit (Fig. 13) for the resonance wavefield filtered at 1.3 Hz is obtained using a fault zone model shown in Fig. 5. The inversion results based on the first higher eigen-mode suggest a fault zone waveguide with ~300-350 m width and ~65% reduction of Vs compared to the host rock (results based on $\chi^2(\tau_0)$ and $\bar{\chi}^2$; Figs. 13 and 14). We also find a strong and robust velocity contrast (~20%; SW faster than NE) across the fault, with opposite sense of the regional contrast observed in previous studies (NE faster than SW; e.g. Allam et al., 2014; Share et al., 2017), which is not resolved by previous modeling of FZTW at the site (Share et al., 2019). Our results imply that the first eigen-mode of resonance waves is sensitive to a secondary low velocity transition zone in the NE. The local reversal of velocity contrast likely reflects asymmetric generation of rock damage on the stiffer (faster) side of the fault by earthquake ruptures with persistent propagation direction. This is consistent with imaging results of the overall velocity contrast across the fault (Allam et al., 2014; Zigone et al., 2015; Share et al., 2019), model simulations of ruptures on a bimaterial interface with the observed regional velocity contrast (e.g., Ben-Zion & Shi, 2005; Xu et al., 2012), geological observations of rock damage asymmetry (Dor et al., 2006) and previous seismlogical observations of fault zone imaging and directivity of small to moderate events in the SJFZ (e.g. Kurzon et al., 2014; Lewis et al., 2005; Meng et al., 2020; Qin et al., 2018; Share et al., 2019).

In general, the distributions of inverted parameters suggest consistent values between the misfit-weighted averages and parameters inferred from the best fitting model, when fitting the two wavefield snapshots independently (results based on misfit $\chi^2(\tau_0)$ and $\chi^2\left(\tau_0 - \frac{\pi}{2\omega}\right)$ from eq. 11; black star and red circle in Figs. 15 and S6). However, the values are inconsistent for results using the same fault zone model to fit both wavefield snapshots (Fig. 13). In addition, models inferred from $\chi^2\left(\tau_0 - \frac{\pi}{2\omega}\right)$ (eq. 11b), misfit of the wavefield snapshot at $\tau_0 - \frac{\pi}{2\omega}$, suggests a fault zone with considerably narrower width (~170 m; Fig. S8a) and smaller Vs reduction (~ 30%; Fig. S8c) that only generates the fundamental eigen-mode. Combined with the inferred smaller velocity contrast (~6%; Fig. S8d), the fundamental eigen-mode is likely more sensitive to the deeper structure, where the fault zone is narrower and the rock damage is more symmetric, compared to the first higher eigen-mode. The fact that at least two different resonance structures are required to explain the observed resonance wavefield snapshots for the lowest peak frequency 1.3 Hz, suggests using a more realistic fault zone model (e.g. four-layer fault zone model as in Ben-Zion (1998) and/or a flower-shape structure) to fit better the observed resonance waves. This is consistent with the spatial variations in peak frequencies of resonance waves measured at different stations within fault zone observed around higher frequencies (2.0 Hz and 2.8 Hz; blue curves in Fig. 4b).

It is intriguing that the modeling of wavefield snapshot at $\tau_0 - \frac{\pi}{2\omega}$ (or the fundamental mode) suggests extremely low β_1 values (~0.6 km/s). This unrealistic low Vs of the host rock may be related to the fact that attenuation is not considered in our analysis, since the attenuation difference within and outside the fault zone (e.g. Lewis et al., 2005; Qiu et al.,

2017) also contributes to the observed amplitude decay outside the fault zone. This effect is less severe for the fitting of the first higher eigen-mode as most of the wavefield snapshot data are within the fault (i.e. wider fault zone). As mentioned in section 4.2, another potential contribution to the obtained unrealistic low β_1 value is that the wavefield snapshot at $\tau_0 - \frac{\pi}{2\omega}$ is likely a summation of both the fundamental and first higher eigen-modes, but it is fitted with only the fundamental mode eigen-function in section 5.2. A future study that includes analyses of attenuation and a transition fault zone layer, and incorporates two different resonance structures for generating the fundamental and first higher modes in the modeling analysis can provide better results.

We demonstrate that the observed resonance waves are sensitive to the same fault zone waveguides, which also generate FZTW that have been analyzed in previous studies (Share et al., 2017, 2019). Fault zone parameters, consistent with those from analyses of FZTW, are obtained independently (i.e. with different frequency and spatial sensitivity kernel) through modeling eigen-functions of the resonance wavefield. This suggests that a joint inversion of FZTW and eigen-functions of resonance waves should yield better constraints on properties of fault damage zones. Better constrained results can be important for a range of topics including ground motion amplification near faults (e.g., Spudich & Olsen, 2001; Rovelli et al. 2002;), directivity of earthquake ruptures (e.g. Ben-Zion & Shi, 2005; Dor et al., 2006) and earthquake cycles (e.g. Thakur et al., 2020).

The modeling results (Section 5) are developed in the context of data generated by an example event (star in Fig. 1) with high SNR at the lowest resonance frequency 1.3 Hz recorded by the BS array. However, similar features are commonly observed in resonance waves for a group of earthquakes recorded by the same set of stations in the BS array (Figs. 3 and S3). It is important to note that this method can also be applied to resonance waves recorded by other dense deployments across faults with long aperture (e.g. a few kilometers). Since the typical width of a fault zone waveguide is less than 500 m (e.g. Lewis & Ben-Zion, 2010; Qin et al., 2018; Share et al., 2019), a station spacing of 30-50 m or less is required for the part of array on the top of the waveguide to sample the resonance wavefield with sufficient spatial resolution (particularly for higher modes). Potential resonance wave signals are also seen in data recorded by other dense linear arrays in the SJFZ (e.g. Figure 4 of Wang et al., 2019). These additional observations may be the subject of a follow up study.

7. Conclusions

The observations and modeling of resonance waves in this study augment the previous fault zone imaging results at the site (e.g. Share et al., 2019) with the following aspects:

1. Resonance waves contain lower frequency contents (< 3 Hz) compared to FZTW (peak at ~5 Hz), and thus provide a different spatial sensitivity to the fault zone waveguide.
2. The wavefield snapshots of resonance modes analyzed in this paper represent the spatial (rather than temporal) variations of trapped energy within a waveguide, and thus have different trade-offs between model parameters compared to those of FZTW modeling (e.g. better resolution of velocity contrast β_3/β_1).
3. Although not modeled in this paper, the observed resonance frequencies (1.3 Hz, 2.0 Hz, and 2.8 Hz; Fig. 4c) may provide additional constraints on the depth of the fault zone waveguide.
4. Since resonance waves at different frequencies and wavefield snapshots dominated by different eigen-modes are sensitive to different aspects of fault zone waveguides, modeling jointly all signals will provide a more comprehensive imaging of fault zone structures.

Acknowledgements

We thank Marianne Karplus and Jerry Schuster for providing geophones for the experiment, and Hsin-Hua Huang, Elizabeth Berg, Yadong Wang, Scott Palmer, Kathleen Ritterbush, Jon Gonzalez, Jerry Schuster, Robert Zinke, and Cooper Harris for assistance during the array deployment. The manuscript benefits from useful comments from two anonymous reviewers, an anonymous Associate Editor and Editor Michael Bostock. The data are available through the International Federation of Digital Seismograph Networks (Allam 2015; https://www.fdsn.org/networks/detail/9K_2015/).

This research was supported by the U.S. Department of Energy (Award #DE-SC0016520), the National Science Foundation (Grant EAR-1753362) and the Southern California Earthquake Center (SCEC publication No. 10153). SCEC is funded by NSF Cooperative Agreement EAR-1600087 and USGS Cooperative Agreement G17AC00047.

References

Allam A. A. (2015): San Jacinto Damage Zone Imaging Arrays. International Federation of Digital Seismograph Networks. Dataset/Seismic Network. 10.7914/SN/9K_2015

Allam, A. A., & Ben-Zion, Y. (2012). Seismic velocity structures in the southern California plate-boundary environment from double-difference tomography. *Geophysical Journal International*, *190*(2), 1181–1196. https://doi.org/10.1111/j.1365-246X.2012.05544.x

Allam, A. A., Ben-Zion, Y., Kurzon, I., & Vernon, F. L. (2014). Seismic velocity structure in the Hot Springs and Trifurcation areas of the San Jacinto fault zone, California, from double-difference tomography. *Geophysical Journal International*, *198*(2), 978–999. https://doi.org/10.1093/gji/ggu176

Avallone, A., Rovelli, A., Di Giulio, G., Improta, L., Ben-Zion, Y., Milana, G., & Cara, F. (2014). Waveguide effects in very high rate GPS record of the 6 April 2009, Mw 6.1 L'Aquila, central Italy earthquake. *Journal of Geophysical Research: Solid Earth*. https://doi.org/10.1002/2013JB010475

Baer, M., & Kradolfer, U. (1987). An automatic phase picker for local and teleseismic events. *Bulletin of the Seismological Society of America*.

Ben-Zion, Y. (1998). Properties of seismic fault zone waves and their utility for imaging low-velocity structures. *Journal of Geophysical Research: Solid Earth*. https://doi.org/10.1029/98jb00768

Ben-Zion, Y., & Aki, K. (1990). Seismic radiation from an SH line source in a laterally heterogeneous planar fault zone. *Bulletin of the Seismological Society of America*.

Ben-Zion, Y., & Sammis, C. G. (2003). Characterization of fault zones. *Pure and Applied Geophysics*. https://doi.org/10.1007/PL00012554

Ben-Zion, Y., & Shi, Z. (2005). Dynamic rupture on a material interface with spontaneous generation of plastic strain in the bulk. *Earth and Planetary Science Letters*. https://doi.org/10.1016/j.epsl.2005.03.025

Ben-Zion, Y., Peng, Z., Okaya, D., Seeber, L., Armbruster, J. G., Ozer, N., et al. (2003). A shallow fault-zone structure illuminated by trapped waves in the Karadere-Duzce branch of the North Anatolian Fault, western Turkey. *Geophysical Journal International*. https://doi.org/10.1046/j.1365-246X.2003.01870.x

Ben-Zion, Y., Vernon, F. L., Ozakin, Y., Zigone, D., Ross, Z. E., Meng, H., et al. (2015). Basic data features and results from a spatially dense seismic array on the San Jacinto fault zone. *Geophysical Journal International*. https://doi.org/10.1093/gji/ggv142

Block, B., Dratler, J., & Moore, R. D. (1970). Earth Normal Modes from a 6.5 Magnitude Earthquake. *Nature*. https://doi.org/10.1038/226343a0

Catchings, R. D., Goldman, M. R., Li, Y. G., & Chan, J. H. (2016). Continuity of the west napa-franklin fault zone inferred from guided waves generated by earthquakes following the 24 august 2014 Mw 6.0 south napa earthquake. *Bulletin of the Seismological Society of America*. https://doi.org/10.1785/0120160154

Cochran, E., Li, Y. G., Shearer, P. M., Barbot, S., Fialko, Y., & Vidale, J. E. (2009). Seismic and geodetic evidence for extensive, long-lived fault damage zones. *Geology*. https://doi.org/10.1130/G25306A.1

Cormier, V. F., & Spudich, P. (1984). Amplification of ground motion and waveform complexity in fault zones: examples from the San Andreas and Calaveras Faults. *Geophysical Journal of the Royal Astronomical Society*. https://doi.org/10.1111/j.1365-246X.1984.tb02846.x

Dor, O., Rockwell, T. K., & Ben-Zion, Y. (2006). Geological observations of damage asymmetry in the structure of the San Jacinto, San Andreas and Punchbowl faults in Southern California: A possible indicator for preferred rupture propagation direction. *Pure and Applied Geophysics*. https://doi.org/10.1007/s00024-005-0023-9

Dziewonski, A. M., & Anderson, D. L. (1981). Preliminary reference Earth model. *Physics of the Earth and Planetary Interiors*. https://doi.org/10.1016/0031-9201(81)90046-7

Ellsworth, W. L., & Malin, P. E. (2011). Deep rock damage in the san andreas fault revealed by P- and S-type fault-zone-guided waves. *Geological Society Special Publication*. https://doi.org/10.1144/SP359.3

Fialko, Y. (2006). Interseismic strain accumulation and the earthquake potential on the southern San Andreas fault system. *Nature*. https://doi.org/10.1038/nature04797

Geimer, P. R., Finnegan, R., & Moore, J. R. (2020). Sparse Ambient Resonance Measurements Reveal Dynamic Properties of Freestanding Rock Arches. *Geophysical Research Letters*, *47*(9), 1–9. https://doi.org/10.1029/2020GL087239

Gilbert, F. (1971). Excitation of the Normal Modes of the Earth by Earthquake Sources. *Geophysical Journal of the Royal Astronomical Society*. https://doi.org/10.1111/j.1365-246X.1971.tb03593.x

Gulley, A. K., Kaipio, J. P., Eccles, J. D., & Malin, P. E. (2017). A numerical approach for modelling fault-zone trapped waves. *Geophysical Journal International*. https://doi.org/10.1093/gji/ggx199

Haberland, C., Agnon, A., El-Kelani, R., Maercklin, N., Qabbani, I., Rümpker, G., et al. (2003). Modeling of seismic guided waves at the Dead Sea Transform. *Journal of Geophysical Research: Solid Earth*. https://doi.org/10.1029/2002jb002309

Hauksson, E., Yang, W., & Shearer, P. M. (2012). Waveform relocated earthquake catalog for Southern California (1981 to June 2011). *Bulletin of the Seismological Society of America*. https://doi.org/10.1785/0120120010

Hillers, G., & Campillo, M. (2018). Fault Zone Imaging from Correlations of Aftershock Waveforms. *Pure and Applied Geophysics*. https://doi.org/10.1007/s00024-018-1836-7

Hillers, G., Campillo, M., Ben-Zion, Y., & Roux, P. (2014). Seismic fault zone trapped noise. *Journal of Geophysical Research: Solid Earth*, *119*(7), 5786–5799. https://doi.org/10.1002/2014JB011217

Jahnke, G., Igel, H., & Ben-Zion, Y. (2002). Three-dimensional calculations of fault-zone-guided waves in various irregular structures. *Geophysical Journal*

International. https://doi.org/10.1046/j.1365-246X.2002.01784.x

Kurzon, I., Vernon, F. L., Ben-Zion, Y., & Atkinson, G. (2014). Ground Motion Prediction Equations in the San Jacinto Fault Zone: Significant Effects of Rupture Directivity and Fault Zone Amplification. *Pure and Applied Geophysics*. https://doi.org/10.1007/s00024-014-0855-2

Lewis, M. A., & Ben-Zion, Y. (2010). Diversity of fault zone damage and trapping structures in the Parkfield section of the San Andreas Fault from comprehensive analysis of near fault seismograms. *Geophysical Journal International*. https://doi.org/10.1111/j.1365-246X.2010.04816.x

Lewis, M. A., Peng, Z., Ben-Zion, Y., & Vernon, F. L. (2005). Shallow seismic trapping structure in the San Jacinto fault zone near Anza, California. *Geophysical Journal International*. https://doi.org/10.1111/j.1365-246X.2005.02684.x

Li, J., Lin, F.-C., Allam, A. A., Ben-Zion, Y., Liu, Z., & Schuster, G. (2019). Wave equation dispersion inversion of surface waves recorded on irregular topography. *Geophysical Journal International*. https://doi.org/10.1093/gji/ggz005

Li, Y. G., Leary, P., Aki, K., & Malin, P. (1990). Seismic trapped modes in the Oroville and San Andreas fault zones. *Science*. https://doi.org/10.1126/science.249.4970.763

Li, Y. G., Aki, K., Adams, D., Hasemi, A., & Lee, W. H. K. (1994). Seismic guided waves trapped in the fault zone of the Landers, California, earthquake of 1992. *Journal of Geophysical Research*. https://doi.org/10.1029/94jb00464

Lindsey, E. O., Sahakian, V. J., Fialko, Y., Bock, Y., Barbot, S., & Rockwell, T. K. (2014). Interseismic Strain Localization in the San Jacinto Fault Zone. *Pure and Applied Geophysics*. https://doi.org/10.1007/s00024-013-0753-z

Malin, P., Shalev, E., Balven, H., & Lewis-Kenedi, C. (2006). Structure of the San Andreas Fault at SAFOD from P-wave tomography and fault-guided wave mapping. *Geophysical Research Letters*. https://doi.org/10.1029/2006GL025973

Mamada, Y., Kuwahara, Y., Ito, H., & Takenaka, H. (2004). Discontinuity of the Mozumi-Sukenobu fault low-velocity zone, central Japan, inferred from 3-D finite-difference simulation of fault zone waves excited by explosive sources. *Tectonophysics*. https://doi.org/10.1016/j.tecto.2003.09.008

Meng, H., McGuire, J. J., & Ben-Zion, Y. (2020). Semi-Automated Estimates of Directivity and Related Source Properties of Small to Moderate Southern California Earthquakes using Second Seismic Moments. *Journal of Geophysical Research: Solid Earth*. https://doi.org/10.1029/2019jb018566

Mizuno, T., & Nishigami, K. Y. (2006). Deep structure of the Nojima Fault, southwest Japan, estimated from borehole observations of fault-zone trapped waves. *Tectonophysics*. https://doi.org/10.1016/j.tecto.2006.01.003

Najdahmadi, B., Bohnhoff, M., & Ben-Zion, Y. (2016). Bimaterial interfaces at the Karadere segment of the North Anatolian Fault, northwestern Turkey. *Journal of Geophysical Research: Solid Earth*. https://doi.org/10.1002/2015JB012601

Peng, Z., Ben-Zion, Y., Michael, A. J., & Zhu, L. (2003). Quantitative analysis of seismic fault zone waves in the rupture zone of the 1992 Landers, California, earthquake: Evidence for a shallow trapping structure. *Geophysical Journal International*. https://doi.org/10.1111/j.1365-246X.2003.02109.x

Prieto, G. A., Parker, R. L., & Vernon, F. L. (2009). A Fortran 90 library for multitaper spectrum analysis. *Computers and Geosciences*.

https://doi.org/10.1016/j.cageo.2008.06.007

Qin, L., Ben-Zion, Y., Qiu, H., Share, P. E., Ross, Z. E., & Vernon, F. L. (2018). Internal structure of the san jacinto fault zone in the trifurcation area southeast of anza, california, from data of dense seismic arrays. *Geophysical Journal International*, *213*(1), 98–114. https://doi.org/10.1093/gji/ggx540

Qiu, H., Ben-Zion, Y., Ross, Z. E., Share, P. E., & Vernon, F. L. (2017). Internal structure of the San Jacinto fault zone at Jackass Flat from data recorded by a dense linear array. *Geophysical Journal International*, *209*(3), 1369–1388. https://doi.org/10.1093/gji/ggx096

Rockwell, T. K., & Ben-Zion, Y. (2007). High localization of primary slip zones in large earthquakes from paleoseismic trenches: Observations and implications for earthquake physics. *Journal of Geophysical Research: Solid Earth*, *112*(10). https://doi.org/10.1029/2006JB004764

Rockwell, T. K., Dawson, T. E., Young Ben-Horin, J., & Seitz, G. (2015). A 21-Event, 4,000-Year History of Surface Ruptures in the Anza Seismic Gap, San Jacinto Fault, and Implications for Long-term Earthquake Production on a Major Plate Boundary Fault. *Pure and Applied Geophysics*, *172*(5), 1143–1165. https://doi.org/10.1007/s00024-014-0955-z

Ross, Z. E., Hauksson, E., & Ben-Zion, Y. (2017). Abundant off-fault seismicity and orthogonal structures in the San Jacinto fault zone. *Science Advances*, https://doi.org/10.1126/sciadv.1601946

Rovelli, A., Caserta, A., Marra, F., & Ruggiero, V. (2002). Can seismic waves be trapped inside an inactive fault zone? The case study of Nocera Umbra, Central Italy. *Bulletin of the Seismological Society of America*. https://doi.org/10.1785/0120010288

Share, P. E., Ben-Zion, Y., Ross, Z. E., Qiu, H., & Vernon, F. L. (2017). Internal structure of the San Jacinto fault zone at Blackburn Saddle from seismic data of a linear array. *Geophysical Journal International*, *210*(2), 819–832. https://doi.org/10.1093/gji/ggx191

Share, P. E., Allam, A. A., Ben-Zion, Y., Lin, F.-C., & Vernon, F. L. (2019). Structural Properties of the San Jacinto Fault Zone at Blackburn Saddle from Seismic Data of a Dense Linear Array. *Pure and Applied Geophysics*, *176*(3), 1169–1191. https://doi.org/10.1007/s00024-018-1988-5

Spudich, P., & Olsen, K. B. (2001). Fault zone amplified waves as a possible seismic hazard along the Calaveras fault in central California. *Geophysical Research Letters*. https://doi.org/10.1029/2000GL011902

Thakur, P., Huang, Y., & Kaneko, Y. (2020). Effects of Low-Velocity Fault Damage Zones on Long-Term Earthquake Behaviors on Mature Strike-Slip Faults. *Journal of Geophysical Research: Solid Earth*. https://doi.org/10.1029/2020JB019587

Wang, Y., Allam, A. A., & Lin, F.-C. (2019). Imaging the Fault Damage Zone of the San Jacinto Fault Near Anza With Ambient Noise Tomography Using a Dense Nodal Array. *Geophysical Research Letters*. https://doi.org/10.1029/2019GL084835

Webb, S. C. (2008). The earth’s hum: The excitation of earth normal modes by ocean waves. *Geophysical Journal International*. https://doi.org/10.1111/j.1365-246X.2008.03801.x

Xu, S., Ben-Zion, Y., & Ampuero, J.-P. (2012). Properties of Inelastic Yielding Zones

Generated by In-plane Dynamic Ruptures: II. Detailed parameter-space study. *Geophysical Journal International*. 191, 1343–1360, https://doi.org/10.1111/j.1365-246X.2012.05685.x.

Yang, H. (2015). Recent advances in imaging crustal fault zones: a review. *Earthquake Science*. https://doi.org/10.1007/s11589-015-0114-3

Yang, H., Zhu, L., & Cochran, E. S. (2011). Seismic structures of the Calico fault zone inferred from local earthquake travel time modelling. *Geophysical Journal International*. https://doi.org/10.1111/j.1365-246X.2011.05055.x

Yang, H., Li, Z., Peng, Z., Ben-Zion, Y., & Vernon, F. (2014). Low-velocity zones along the San Jacinto Fault, Southern California, from body waves recorded in dense linear arrays. *Journal of Geophysical Research: Solid Earth*. https://doi.org/10.1002/2014JB011548

Zigone, D., Ben-Zion, Y., Campillo, M., & Roux, P. (2015). Seismic Tomography of the Southern California Plate Boundary Region from Noise-Based Rayleigh and Love Waves. *Pure and Applied Geophysics*, *172*(5), 1007–1032. https://doi.org/10.1007/s00024-014-0872-1

Figure 1. (a) Location map for the San Jacinto fault zone (SJFZ) with surface traces of major faults (black lines) and seismicity (circles with size proportional to magnitude) during the 35 days recording period. The green triangle and square denote locations of the BS fault zone array and the town of Anza, respectively. The blue rectangle outlines earthquakes (colored by depth) analyzed in this study, whereas events outside the box are shown as gray circles. The yellow star marks location of the example event (Mw 2.98; seismograms shown in Fig. 2) that is used to infer local fault zone parameters through modeling of fault zone resonance wave (Section 5). Waveforms of the event marked as a yellow diamond are shown in Fig. S1. (b) A zoom in of the BS array configuration (red triangles) with green star representing station BS55 that is nearest to the surface trace of Clark fault, the main segment of San Jacinto fault. (c) Location map for the Southern California boundary region. The red box outlines the study area and green triangle denotes the BS array. The purple line (AA') depicts the assumed fault strike for waveform rotation. SAF = San Andreas Fault; EF = Elsinore Fault; SJF = San Jacinto Fault.

Figure 2. Vertical (left) and fault parallel (right) component recordings bandpass filtered between 0.5 and 20 Hz for the target event marked as the yellow star in Fig. 1a. Blue dashed lines indicate the array-mean *S* wave arrival time, whereas red dashed lines denote the snapshot time of Fig. 3a, i.e. ~3 s after the blue dashed lines or "1.52s relative to maximum" of Animation 2, for the target event. The fault normal distance is calculated relative to station BS55 with positive representing the NE. The *P* waveforms are much larger on the vertical component, while the *S* waveforms are more pronounced on the fault parallel component. The white gaps signify lack of data (problematic recordings). Stations with fault-damage-zone amplified (higher amplitudes and longer durations) *S* waves are detected (Text S2) and observed in a ~500 m wide zone marked by the blue solid line.

Figure 3. (a) Snapshots of vertical component wavefield for different events at t_i, ~3 s after the array-mean *S* wave arrival time *i*-th earthquake, recorded on the entire array (snapshot of Animation 2 at ~1.5 s). In addition to the preprocessing steps described in section 2, the shown waveforms are further lowpass filtered at 5 Hz.

Only events that generate *S* waves with enough quality at vertical component are shown. The color illustrates the normalized amplitude (vertical axis) with red and blue representing positive and negative values. The fault normal distance is calculated relative to station BS55 with positive representing the NE. Consistent spatial wavefield pattern is observed for snapshots of all analyzed events. (b) Percentage of events as a function of station location, where fault zone resonance waves are identified in the fault parallel component *S* waveforms (circles and solid curve; Text S2). The blue bar outlines a 500 m wide zone where event percentage are higher than 80% (black dashed lines). ~120 events with sufficient quality (SNR > 10) *S* waves are analyzed here. (c) Average shear wave velocity (Vs; circles) as a function of the array-median hypocenter distance for events with signal to noise ratio higher than 10. The average Vs of the closest 10 events are colored in red and outlined by the black box.

Figure 4. (a) Fault-parallel component waveforms after applying the integration and convolution described in Section 3 to seismograms shown in Fig. 2b. Waveforms 2s before the *S* arrival are truncated to better illustrate the S-waves (at ~22s) together with the subsequent fault zone reflected/converted (black box) and resonance (red box) waves. The black dashed lines illustrate the time window used to compute amplitude spectra, which begin later than the red box to include the resonance waves but exclude the reflected/converted phase and longer to achieve high resolution in frequency domain for spectrum calculation. (b) Amplitude spectra for all waveforms between the black dashed lines in (a). Multi-taper method (Prieto et al., 2009) is used to compute the amplitude spectra. Amplitude spectra for waveforms recorded by stations within the red box in (a) are colored in blue. Three peak resonance frequencies, centered around 1.3 Hz, 2.0 Hz, and 2.8 Hz, of the amplitude spectrum averaged over all the blue amplitude spectra, red curve in (c), are illustrated as red, blue, and green dashed lines. Zero fault normal distance denotes location of the station BS55. (c) The red curve represents the mean of all the blue amplitude spectra in (b). The dashed lines denote the three dominate frequency peaks of the red curve.

Figure 5. A fault zone model with a vertical low velocity layer between two quarter-spaces (modified from Ben-Zion et al., 2003). The perturbation source (circle) is an *SH* line dislocation with coordinates (x_s, z_s). W and β denote the fault zone width and shear wave velocities, respectively. Attenuation is not included in this model. The blue arrows illustrate the coordinate system used in the equation derivation.

Figure 6. Fault zone resonance wavefield before (left) and after (right) smoothing & topographic correction using a reference Vs of 2 km/s. The wavefield is narrow bandpass filtered at 1.3 Hz. The color, same as in Fig. 8b, represents the normalized wavefield. The black curve in the right panel shows $\rho(t)$ (eq. 9b), whereas the black and red dashed lines denote $t = \tau_0 - \frac{\pi}{2\omega}$ and τ_0 (eq. 9a). The horizontal gray dashed lines outline the stations with maximum amplitude larger than 35% of the maximum of the entire wavefield. The wavefield snapshots at $t = \tau_0 - \frac{\pi}{2\omega}$ and τ_0 are depicted in Fig. 7.

Figure 7. Snapshots of wavefield shown in Fig. 6b at lapse times $\tau_0 - \frac{\pi}{2\omega}$ (black curve) and τ_0 (red curve). The topography beneath the array is depicted as the gray dashed curve. Green and blue dashed curves correspond to results using 1.5 km/s and 3 km/s as the reference velocity for topographic correction, respectively. The shaded area illustrates the estimated uncertainty of the extracted wavefield snapshot.

Figure 8. Phase velocities (a) and synthetic total displacement wavefield in time domain (b) solved for resonance waves at 3 Hz. A fault zone model (Fig. 5) with W = 400 m, β_1 = 2.0 km/s, β_3/β_1 = 1.03, and β_2/β_1 = 0.45 is used. The perturbation source is located at x_0 = 0 (red star) and z_0 = 1.5 km. Density is set to be 2700 kg/m^3 and the wavefield in the right panel is normalized by the maximum value. The *x*-axis of (a) denotes $X = W\omega\sqrt{\beta_2^{-2} - c^{-2}}$ (eq. 6). The black and red curves illustrate the left- and right-hand sides of equation 6. The *y*-axis of (b) denotes the phase ωt. The black dashed lines in (b) illustrate the boundaries of the assumed fault zone layer. LHS – left hand side of equation 6; RHS – right hand side of equation 6; $\omega = 2\pi/3$ – angular frequency.

Figure 9. (a) Wavefield snapshot at the time of the maximum of the entire wavefield (top) and eigen-functions of resonance waves at 3 Hz. The corresponding phase shifts relative to the station located at -400 m are shown in (b). The dashed vertical lines denote the boundaries of the assumed fault zone layer (Fig. 5).

Figure 10. (a) Synthetic total displacement wavefield in time domain solved for resonance waves at 3 Hz. The fault zone model of Fig. 8 is used, but the perturbation source is placed at a location that satisfies $R_0' = R_0$, $R_1' = 0.2R_1e^{i\pi/5}$, and $R_2' = 0$. The horizontal black dashed lines outline the fault zone edges, while the black curve depicts $\rho(t)$ (eq. 9b). Red and green vertical dashed lines indicate time instances of τ_0 and $\tau_0 - \frac{\pi}{2\omega}$ (eq. 9a), respectively. (b) Same as (a) but for $R_1' = 0.2R_1e^{i\pi/2}$.

Figure 11. (a) Snapshots of the wavefield shown in Fig. 10a at lapse times τ_0 (red) and $\tau_0 - \frac{\pi}{2\omega}$ (green). Eigen-functions of the fundamental and first higher resonance mode are shown in blue and black dashed curves, respectively. (b) Same as (a) but for Fig. 10b.

Figure 12. Misfit histograms for (a) $\bar{\chi}^2$ (eq. 11c), (b) $\chi^2(\tau_0)$ (eq. 11a), and (c) $\chi^2\left(\tau_0 - \frac{\pi}{2\omega}\right)$ (eq. 11b). The number of models with misfit values less than 13 is shown on the top left corner.

Figure 13. Fault zone resonance wave modeling results. (a) Blue curve indicates $V(x, \tau_0; \omega)$ with dashed curves indicating the uncertainty. The synthetic wavefield snapshot of the best fitting model is shown in red and the corresponding fault zone parameters are shown in the left bottom corner of (b). The gray shaded area represents all synthetics with a $\bar{\chi}^2(\tau_0)$ value less than 1.5 times $\min[\bar{\chi}^2(\tau_0)]$. The fault zone parameters of these selected models are illustrated in Fig. 14. (b) Same as (a) for $V\left(x, \tau_0 - \frac{\pi}{2\omega}; \omega\right)$. (c) Same as (a) but using $\chi^2(\tau_0)$ for model selection. (d) Same as (b) but using $\chi^2\left(\tau_0 - \frac{\pi}{2\omega}\right)$ for model selection.

Figure 14 Parameter spaces as a function of misfit $\bar{\chi}^2$ defined in equation 10c. (a) Fault zone width *W*. Each green circle denotes one fault zone model that has $\bar{\chi}^2 \leq$

$1.5 \cdot \min(\bar{\chi}^2)$ with x and y axes showing corresponding values of fault zone width and misfit, respectively. The best fitting model width is indicated by the red dot, and the black star denotes average model width weighted by the misfit values (eq. 12). (b) Same as (a) for β_1. (c) Same as (a) for β_2/β_1. (d) Same as (a) for β_3/β_1. The misfit-weighted average values of fault zone parameters shown on the top left are rounded to 1 m in (a), 0.01 km/s in (b), and 1% in (c) & (d).

Figure 15. Parameter spaces as a function of misfit $\chi^2(\tau_0)$ defined in equation 11a.

Figure 1.

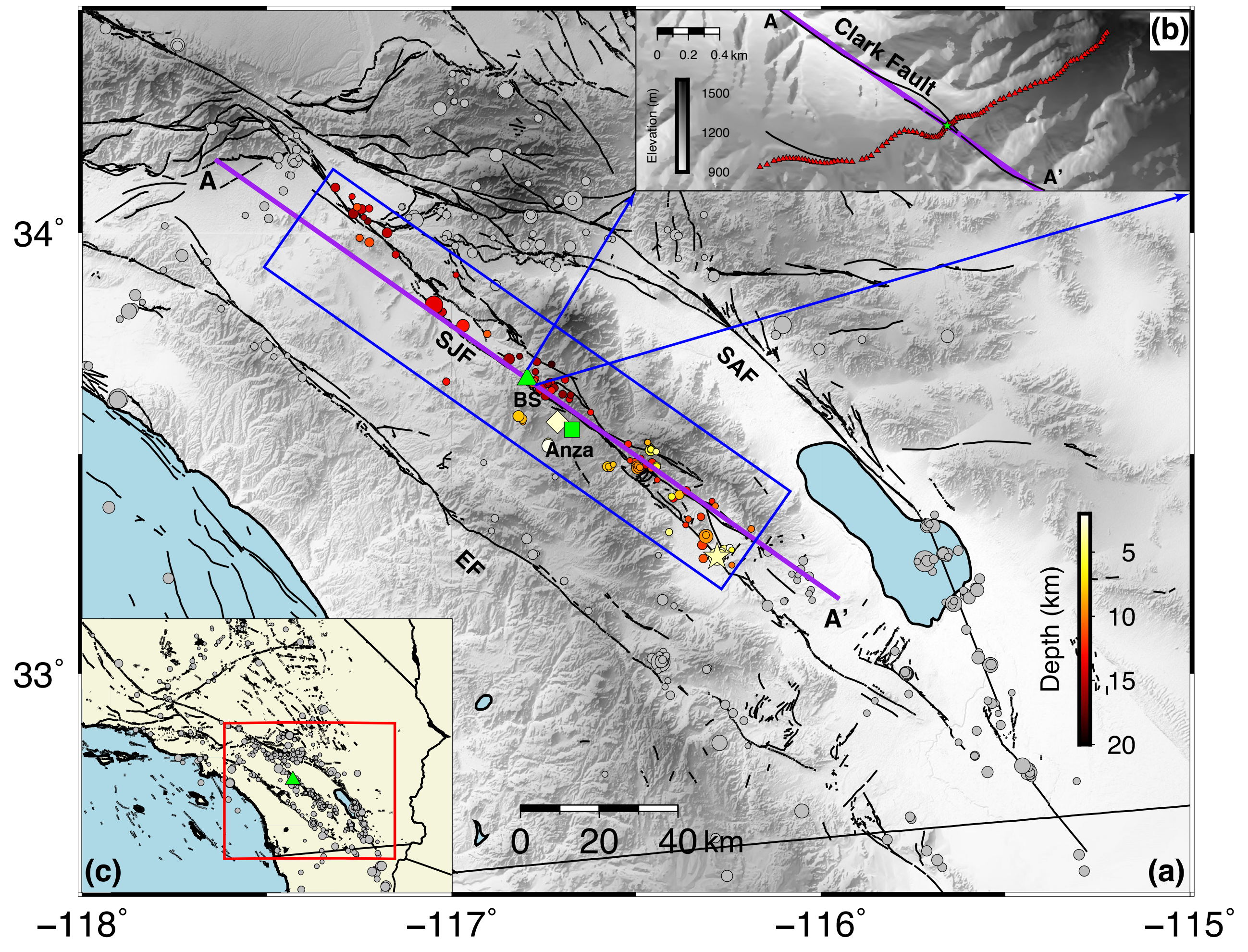

(a)
(b)
(c)
A
A'
SJF
SAF
EF
BS
Anza
Clark Fault
0 0.2 0.4 km
Elevation (m)
1500
1200
900
Depth (km)
5
10
15
20
0 20 40 km
34°
33°
−118°
−117°
−116°
−115°

Figure 2.

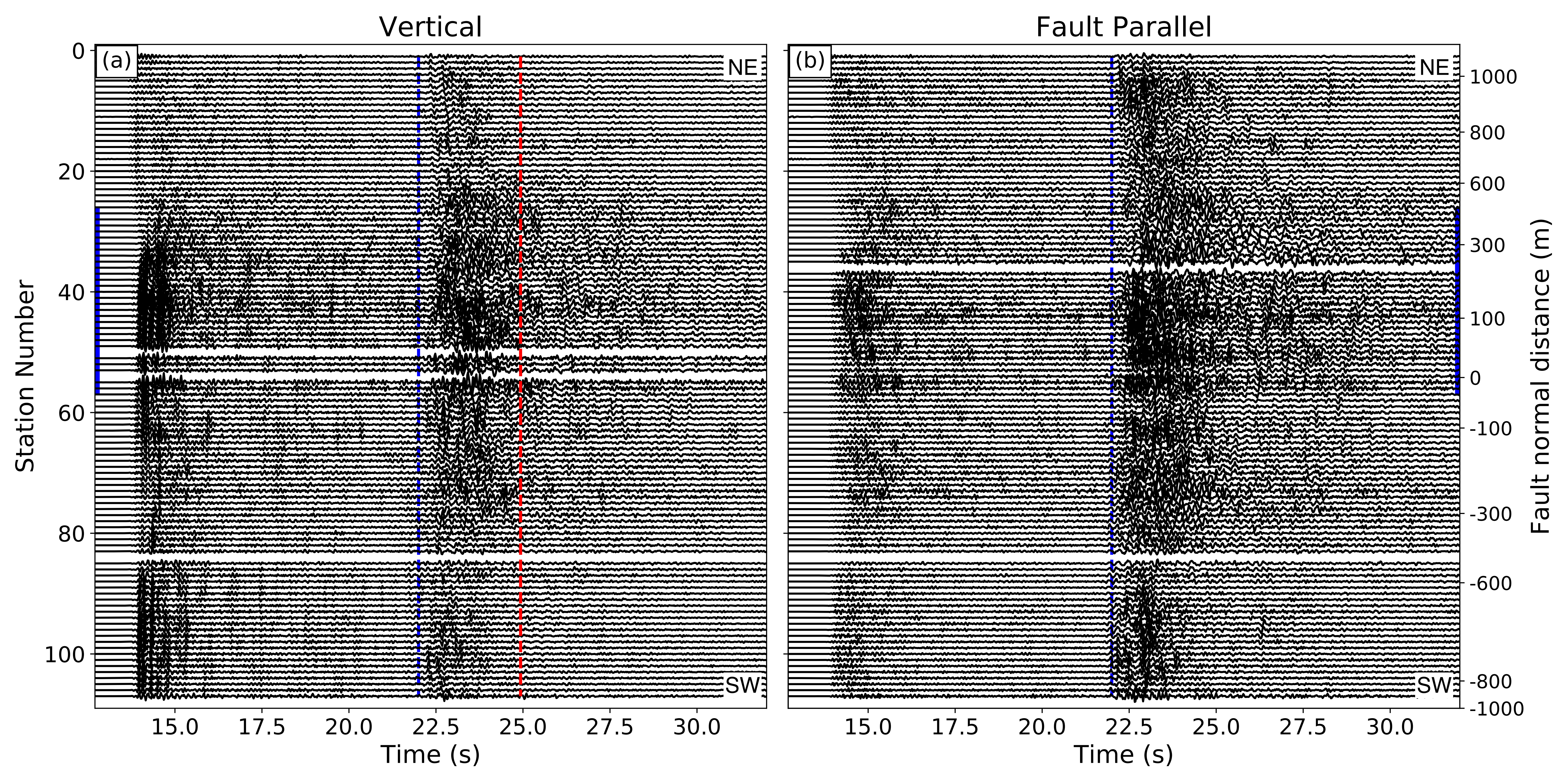

Vertical
Fault Parallel
(a)
(b)
NE
SW
Station Number
Time (s)
Fault normal distance (m)
0
20
40
60
80
100
15.0
17.5
20.0
22.5
25.0
27.5
30.0
1000
800
600
300
100
0
-100
-300
-600
-800
-1000

Figure 3.

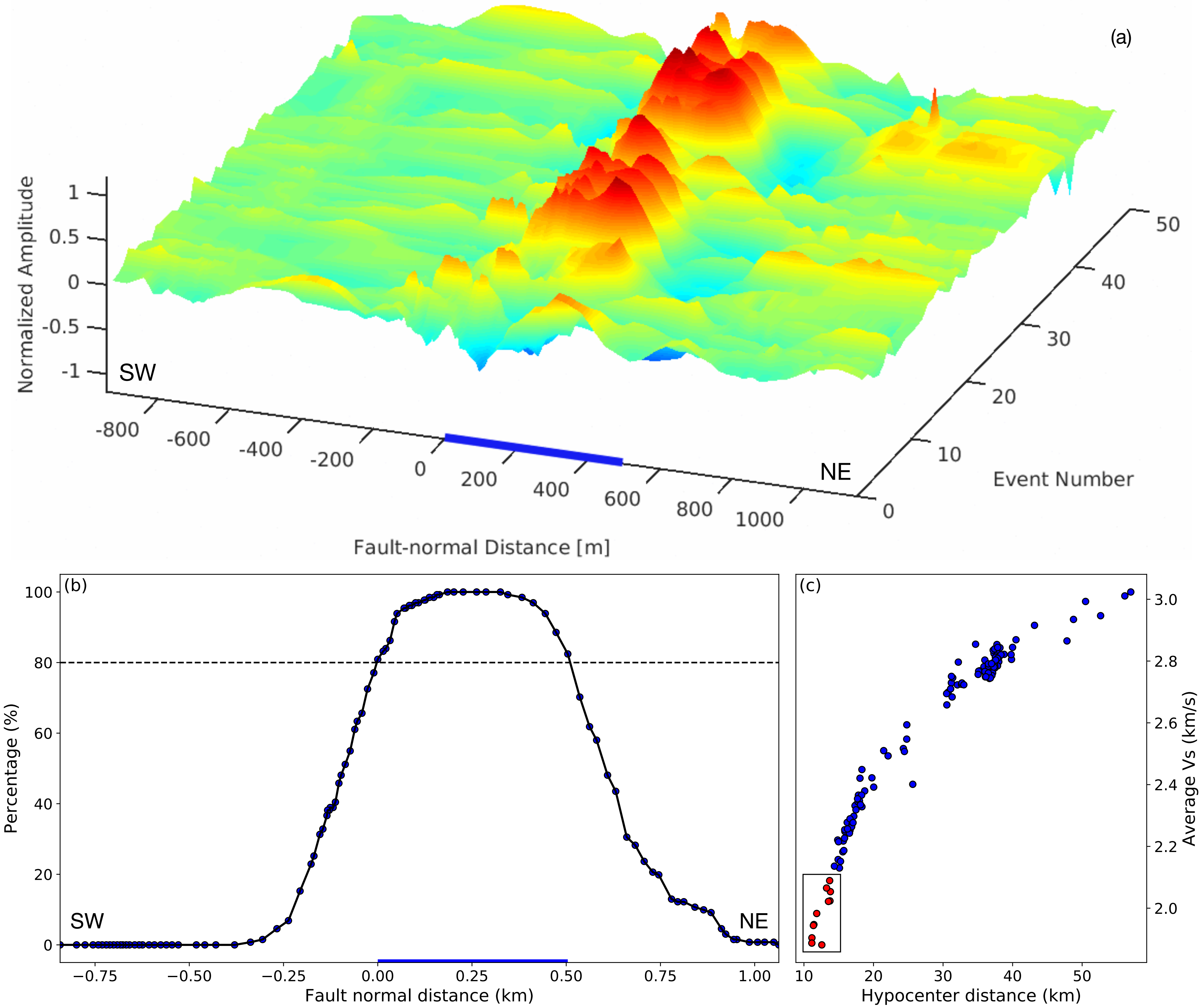

(a)
Normalized Amplitude
1
0.5
0
-0.5
-1
SW
NE
-800
-600
-400
-200
0
200
400
600
800
1000
Fault-normal Distance [m]
0
10
20
30
40
50
Event Number
(b)
Percentage (%)
100
80
60
40
20
0
SW
NE
−0.75
−0.50
−0.25
0.00
0.25
0.50
0.75
1.00
Fault normal distance (km)
(c)
3.0
2.8
2.6
2.4
2.2
2.0
Average Vs (km/s)
10
20
30
40
50
Hypocenter distance (km)

Figure 4.

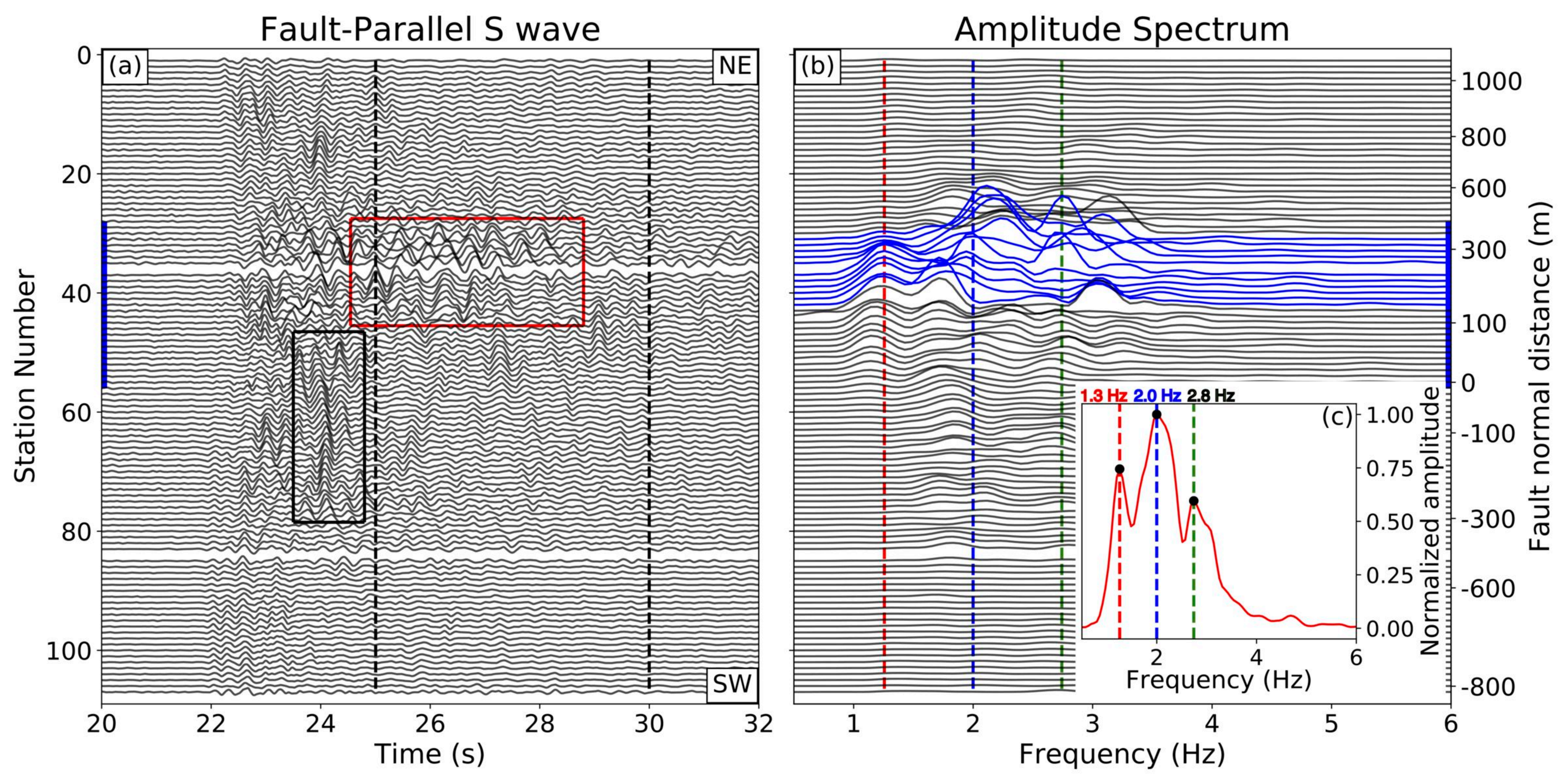

Fault-Parallel S wave
Amplitude Spectrum
(a)
(b)
(c)
NE
SW
Station Number
Time (s)
Frequency (Hz)
Fault normal distance (m)
1.3 Hz
2.0 Hz
2.8 Hz
Normalized amplitude

Figure 5.

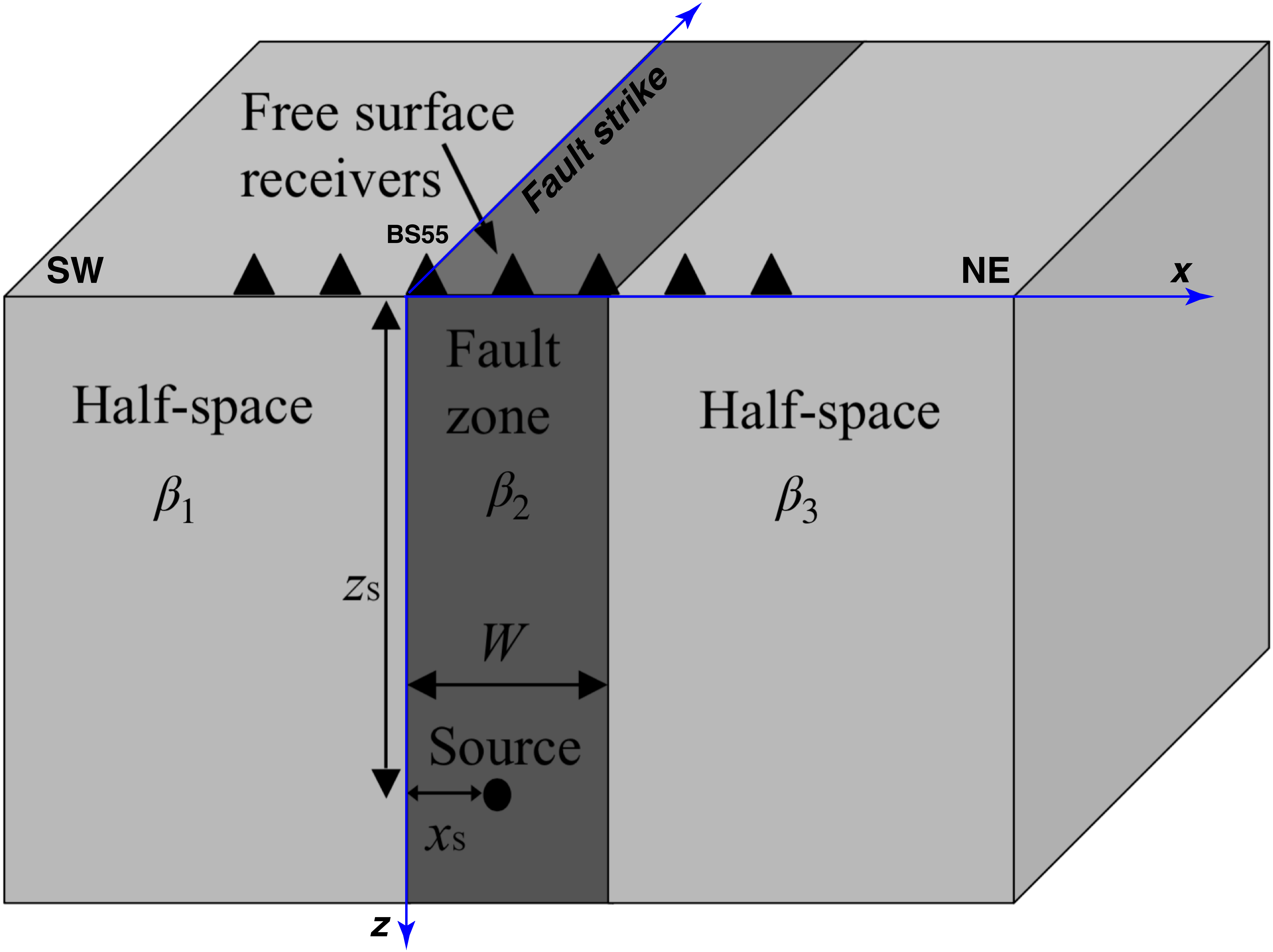

Free surface
receivers
Fault strike
BS55
SW
NE
x
Fault
zone
Half-space
Half-space
β_1
β_2
β_3
z_s
W
Source
x_s
z

Figure 6.

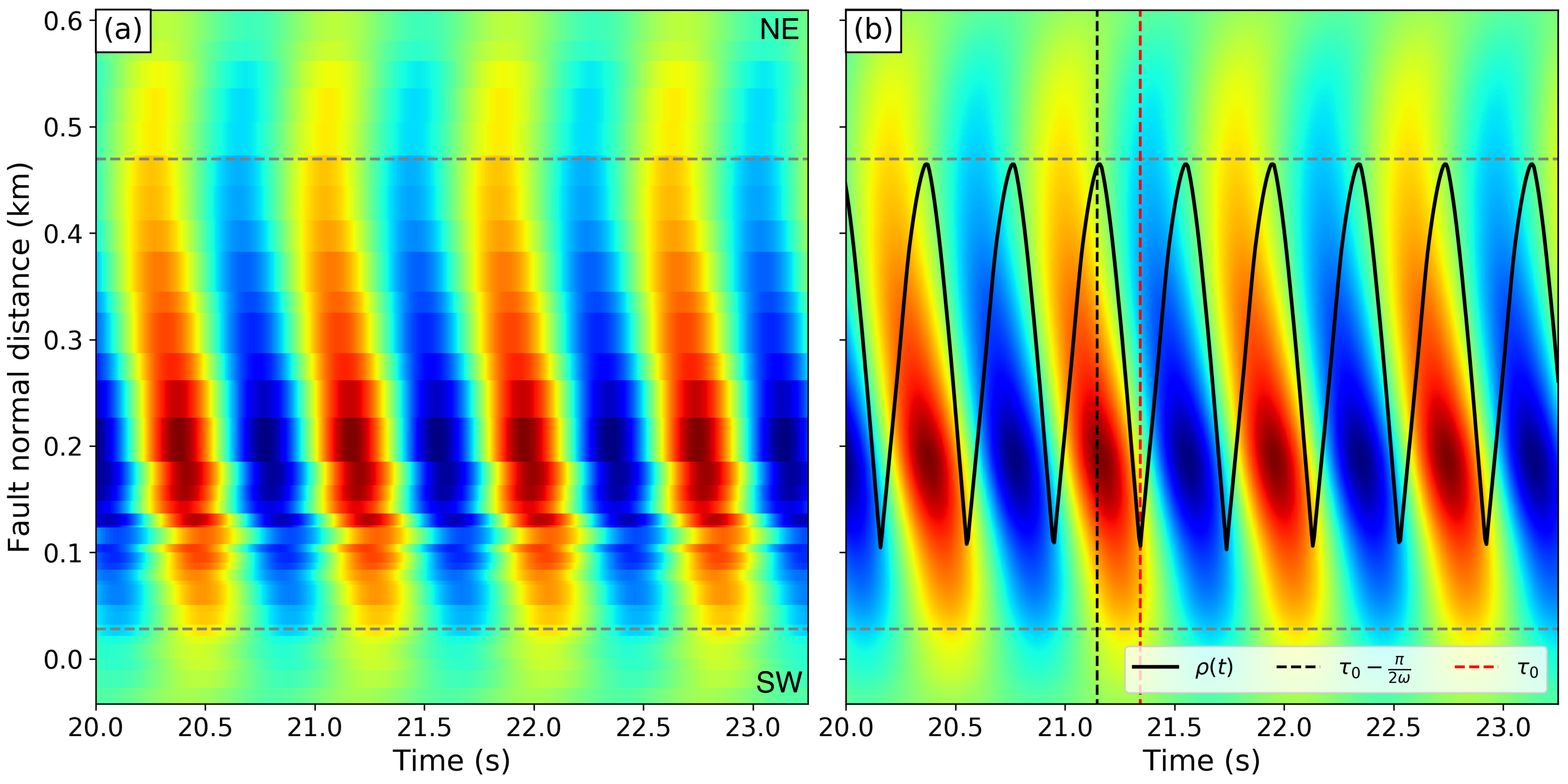

(a)
NE
SW
Fault normal distance (km)
0.6
0.5
0.4
0.3
0.2
0.1
0.0
20.0
20.5
21.0
21.5
22.0
22.5
23.0
Time (s)
(b)
$\rho(t)$
$\tau_0 - \frac{\pi}{2\omega}$
τ_0
20.0
20.5
21.0
21.5
22.0
22.5
23.0
Time (s)

Figure 7.

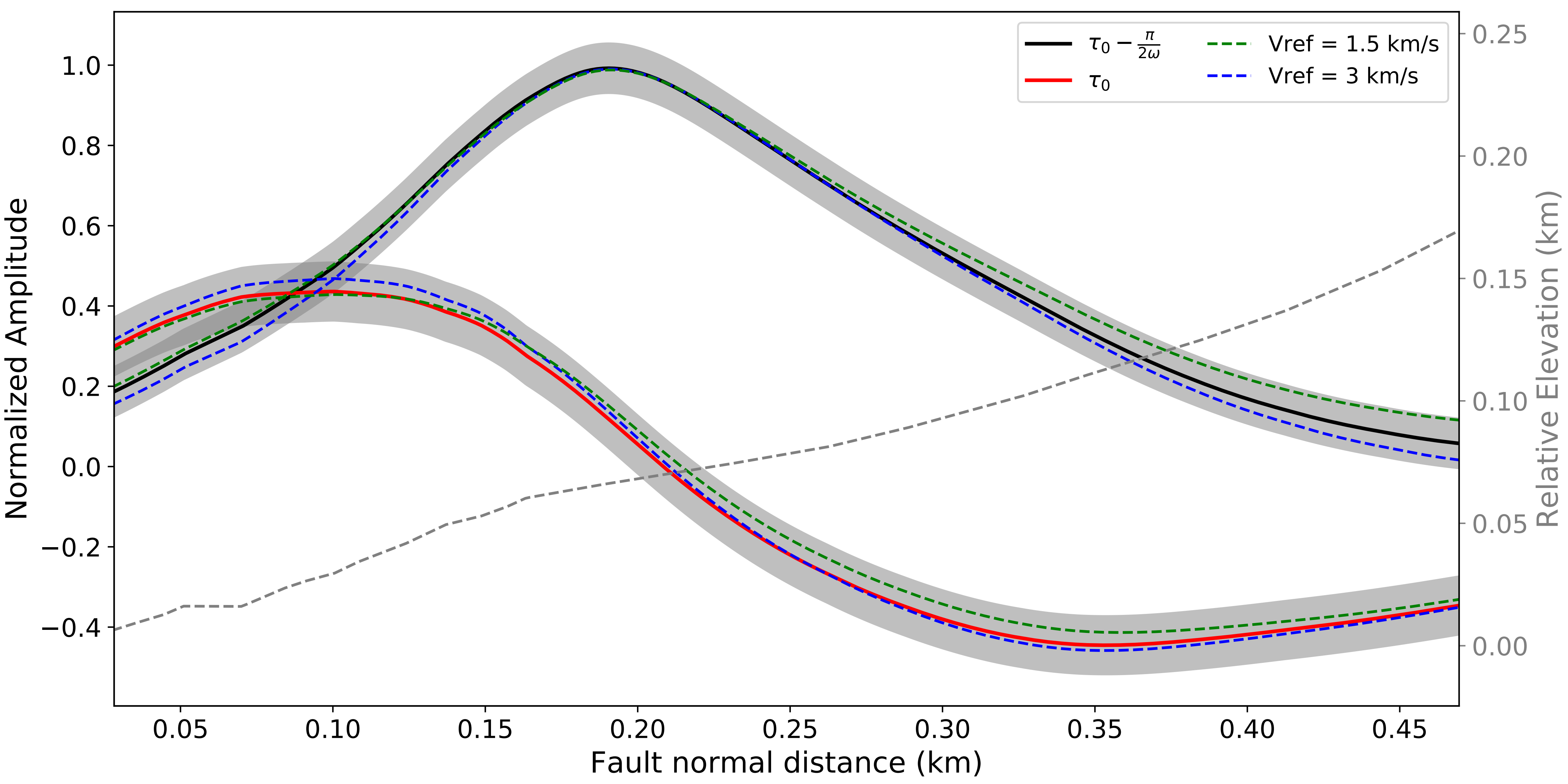

$\tau_0 - \frac{\pi}{2\omega}$
τ_0
Vref = 1.5 km/s
Vref = 3 km/s
Normalized Amplitude
Relative Elevation (km)
Fault normal distance (km)
1.0
0.8
0.6
0.4
0.2
0.0
−0.2
−0.4
0.25
0.20
0.15
0.10
0.05
0.00
0.05
0.10
0.15
0.20
0.25
0.30
0.35
0.40
0.45

Figure 8.

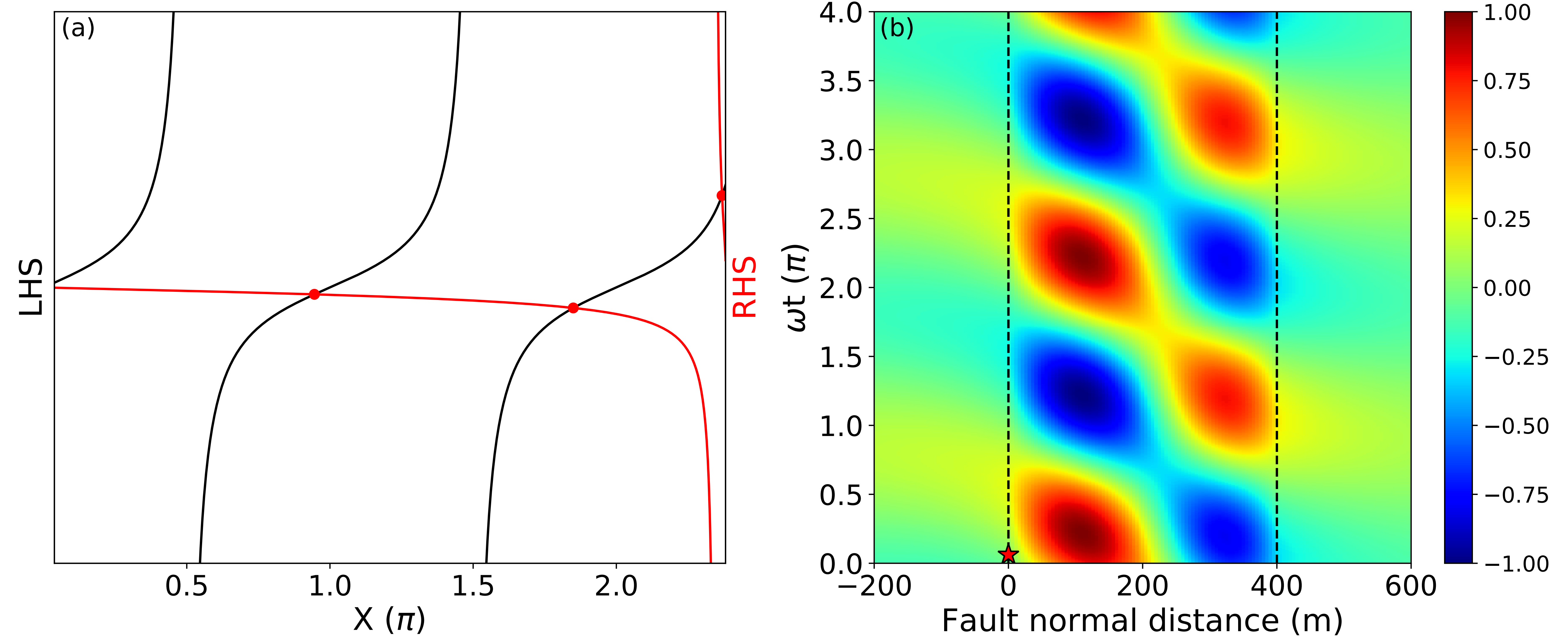
(a)
LHS
RHS
0.5
1.0
1.5
2.0
X (π)
(b)
4.0
3.5
3.0
2.5
2.0
1.5
1.0
0.5
0.0
ωt (π)
−200
0
200
400
600
Fault normal distance (m)
1.00
0.75
0.50
0.25
0.00
−0.25
−0.50
−0.75
−1.00

Figure 9.

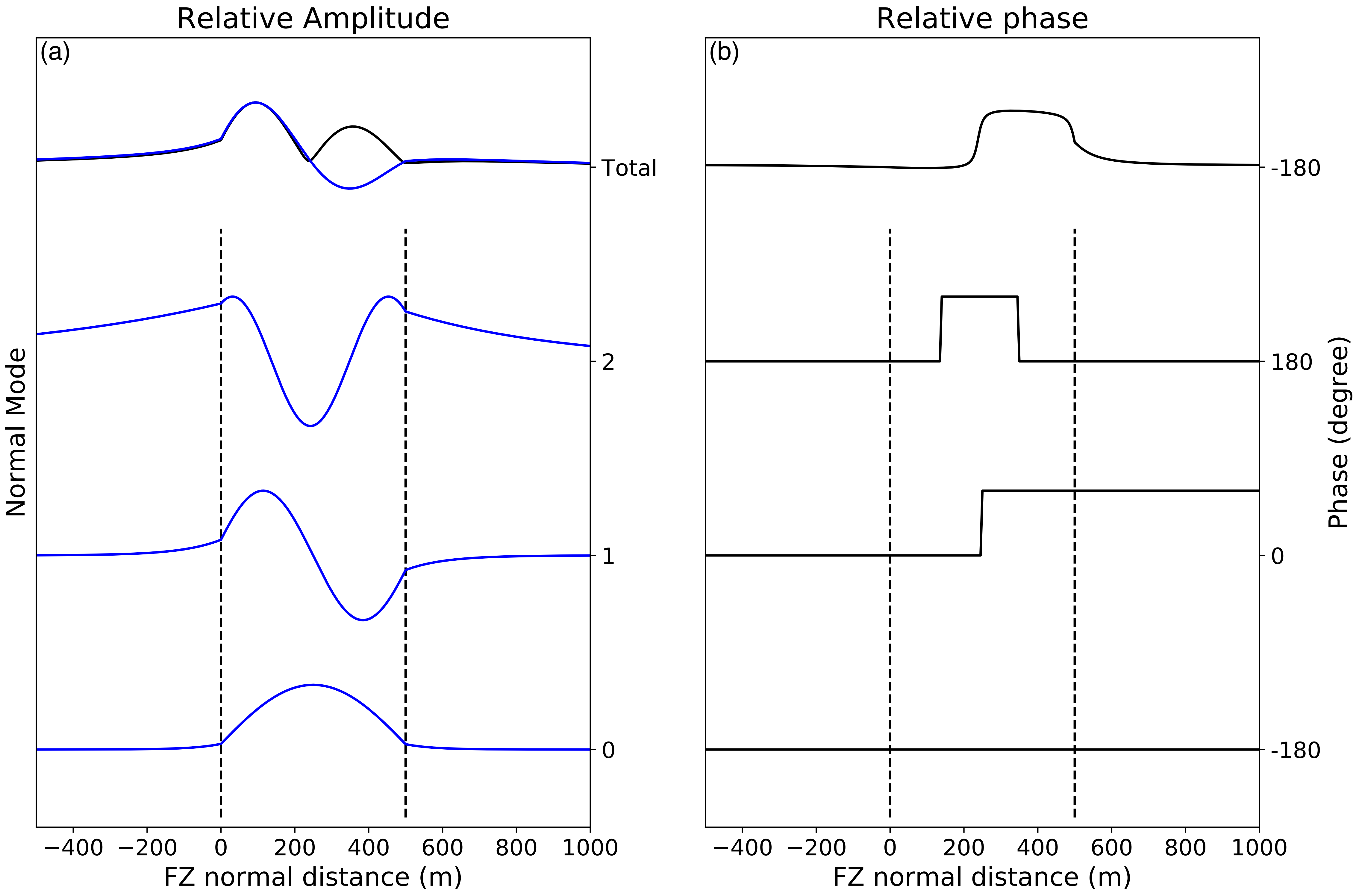

Relative Amplitude
(a)
Total
2
1
0
Normal Mode
−400
−200
0
200
400
600
800
1000
FZ normal distance (m)
Relative phase
(b)
-180
180
0
-180
Phase (degree)
−400
−200
0
200
400
600
800
1000
FZ normal distance (m)

Figure 10.

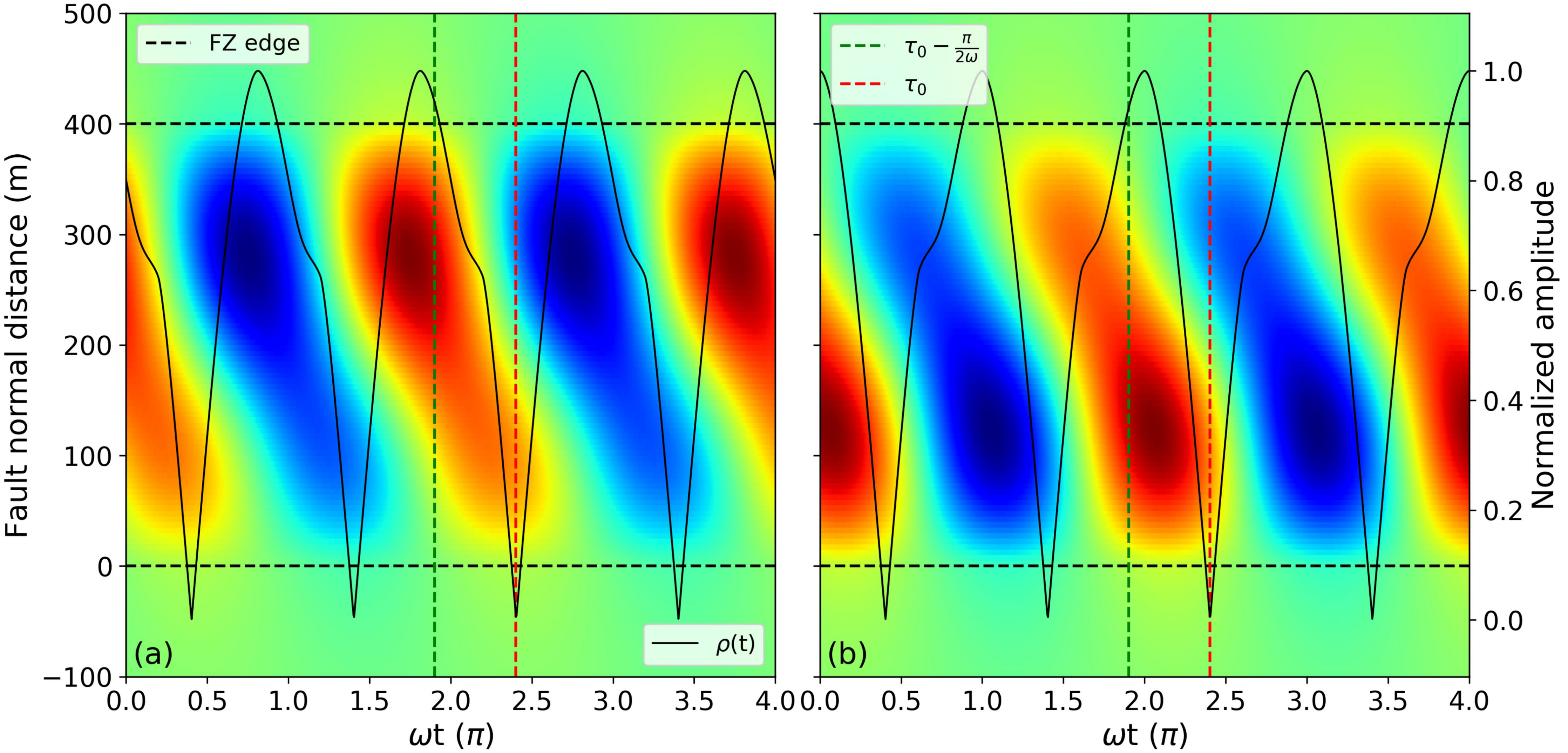

FZ edge
ρ(t)
(a)
Fault normal distance (m)
ωt (π)
$\tau_0 - \frac{\pi}{2\omega}$
τ_0
(b)
Normalized amplitude
500
400
300
200
100
0
−100
0.0
0.5
1.0
1.5
2.0
2.5
3.0
3.5
4.0
0.2
0.4
0.6
0.8

Figure 11.

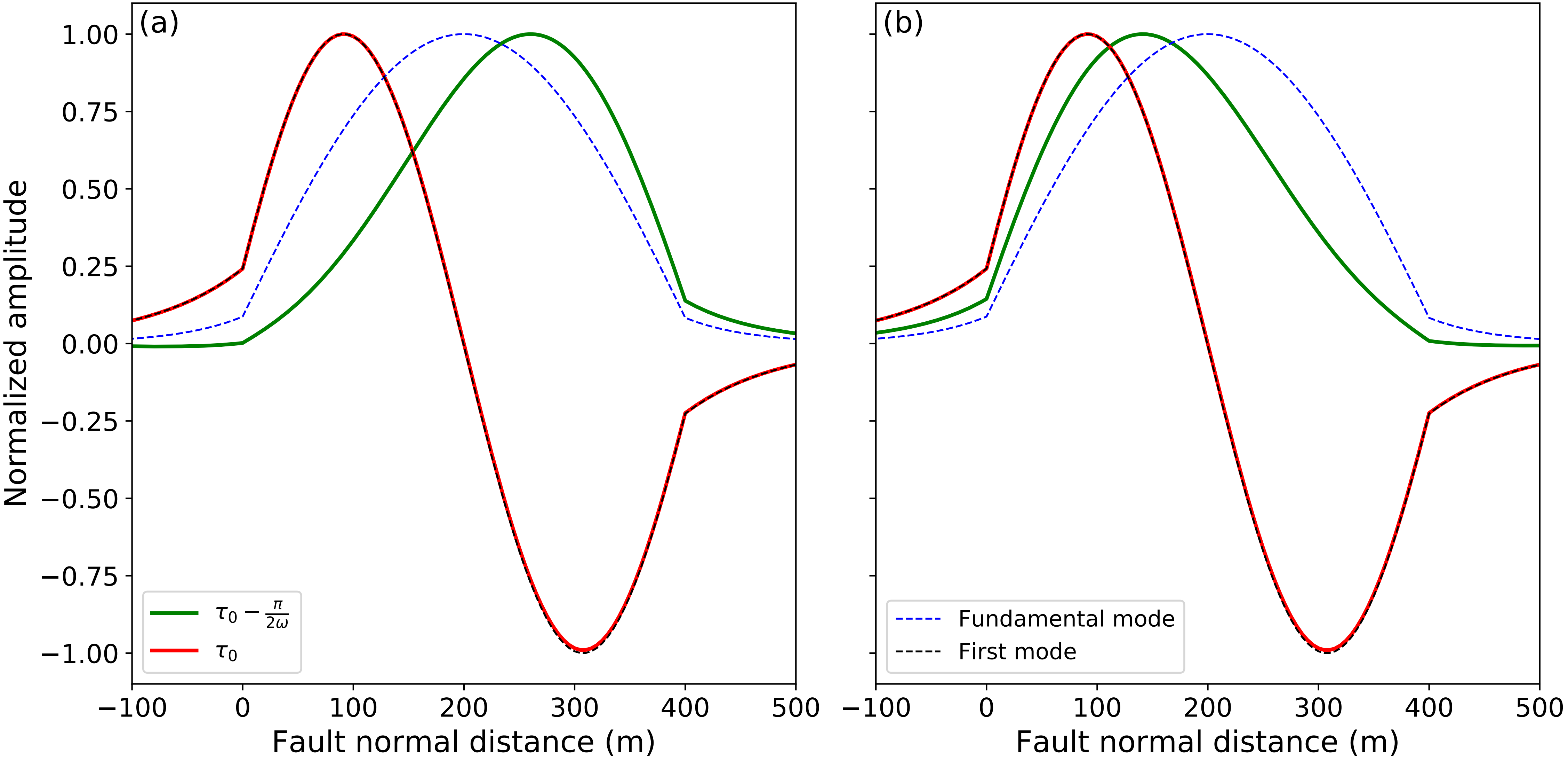

(a)
(b)
Normalized amplitude
Fault normal distance (m)
Fault normal distance (m)
1.00
0.75
0.50
0.25
0.00
−0.25
−0.50
−0.75
−1.00
−100
0
100
200
300
400
500
$\tau_0 - \frac{\pi}{2\omega}$
τ_0
Fundamental mode
First mode

Figure 12.

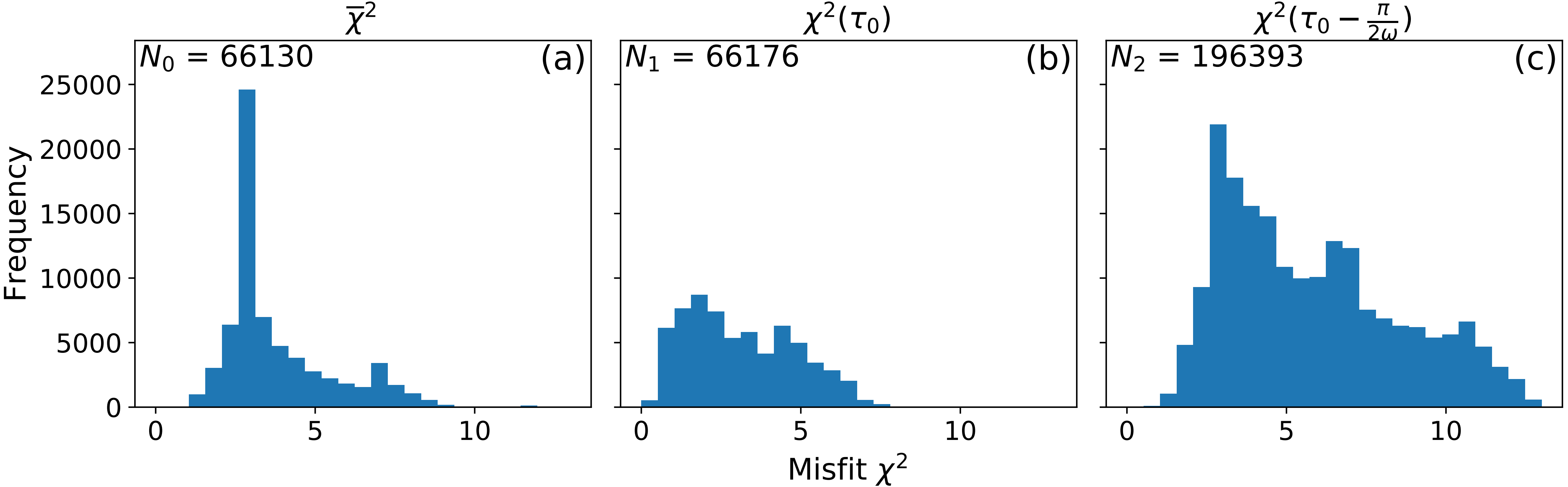
$\overline{\chi}^2$
$\chi^2(\tau_0)$
$\chi^2(\tau_0 - \frac{\pi}{2\omega})$
N_0 = 66130
(a)
N_1 = 66176
(b)
N_2 = 196393
(c)
Frequency
25000
20000
15000
10000
5000
0
0
5
10
Misfit χ^2

Figure 13.

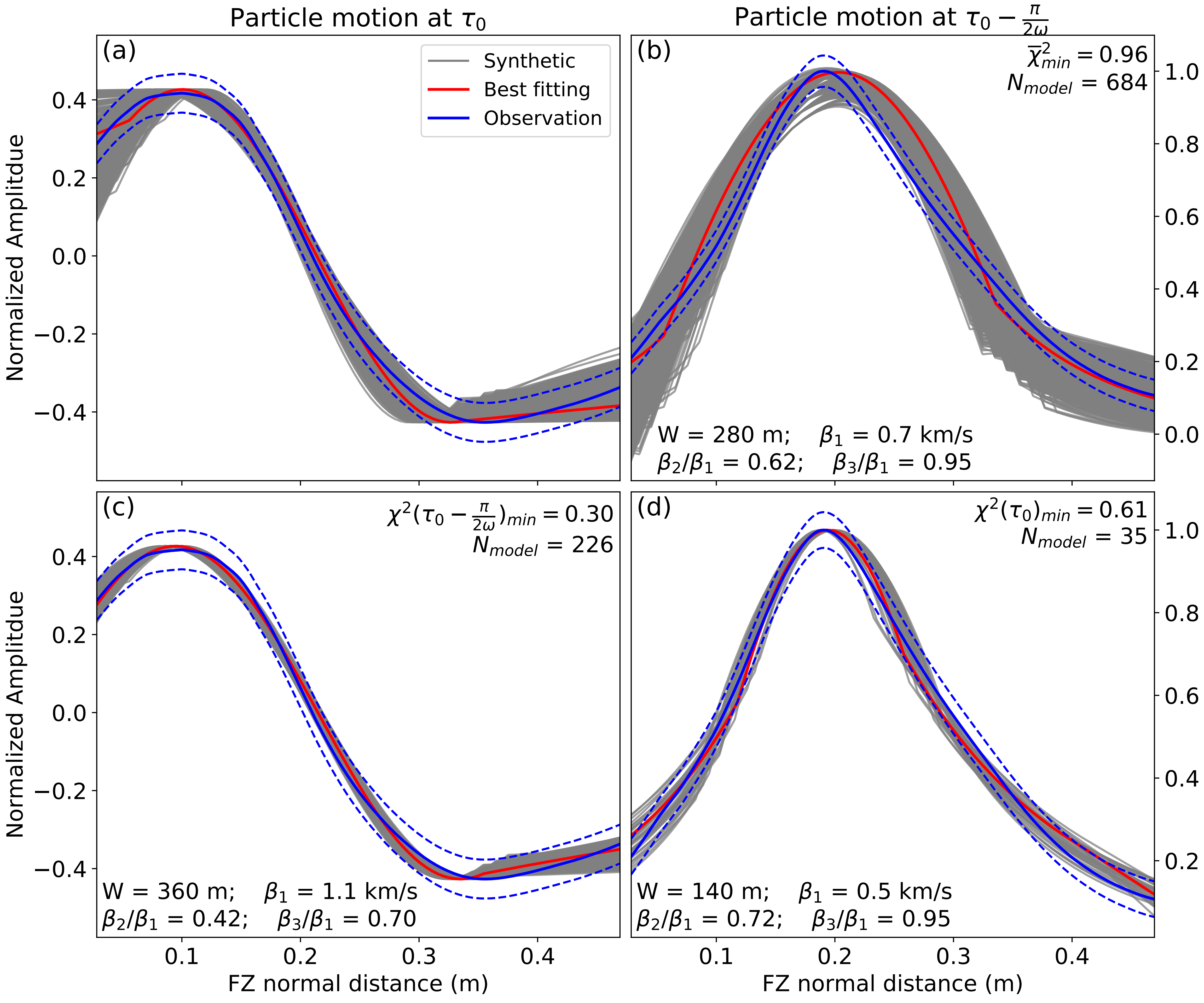

Particle motion at τ_0
Particle motion at $\tau_0 - \frac{\pi}{2\omega}$
(a)
Synthetic
Best fitting
Observation
(b)
$\overline{\chi}^2_{min} = 0.96$
N_{model} = 684
W = 280 m; β_1 = 0.7 km/s
β_2/β_1 = 0.62; β_3/β_1 = 0.95
(c)
$\chi^2(\tau_0 - \frac{\pi}{2\omega})_{min} = 0.30$
N_{model} = 226
W = 360 m; β_1 = 1.1 km/s
β_2/β_1 = 0.42; β_3/β_1 = 0.70
(d)
$\chi^2(\tau_0)_{min} = 0.61$
N_{model} = 35
W = 140 m; β_1 = 0.5 km/s
β_2/β_1 = 0.72; β_3/β_1 = 0.95
Normalized Amplitdue
FZ normal distance (m)

Figure 14.

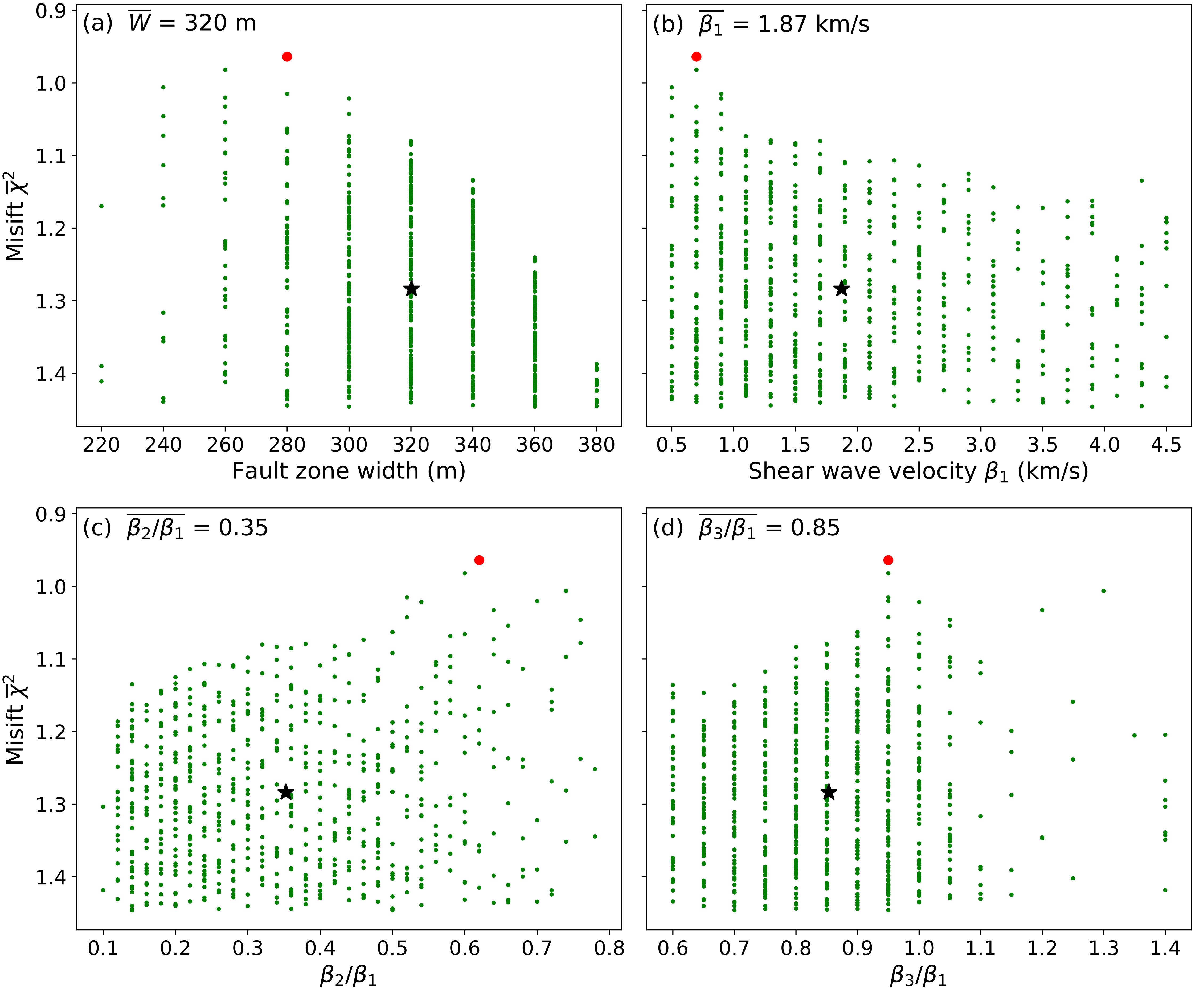
(a) $\overline{W}$ = 320 m
(b) $\overline{\beta_1}$ = 1.87 km/s
(c) $\overline{\beta_2/\beta_1}$ = 0.35
(d) $\overline{\beta_3/\beta_1}$ = 0.85
Misfit $\overline{\chi}^2$
Fault zone width (m)
Shear wave velocity β_1 (km/s)
β_2/β_1
β_3/β_1

Figure 15.

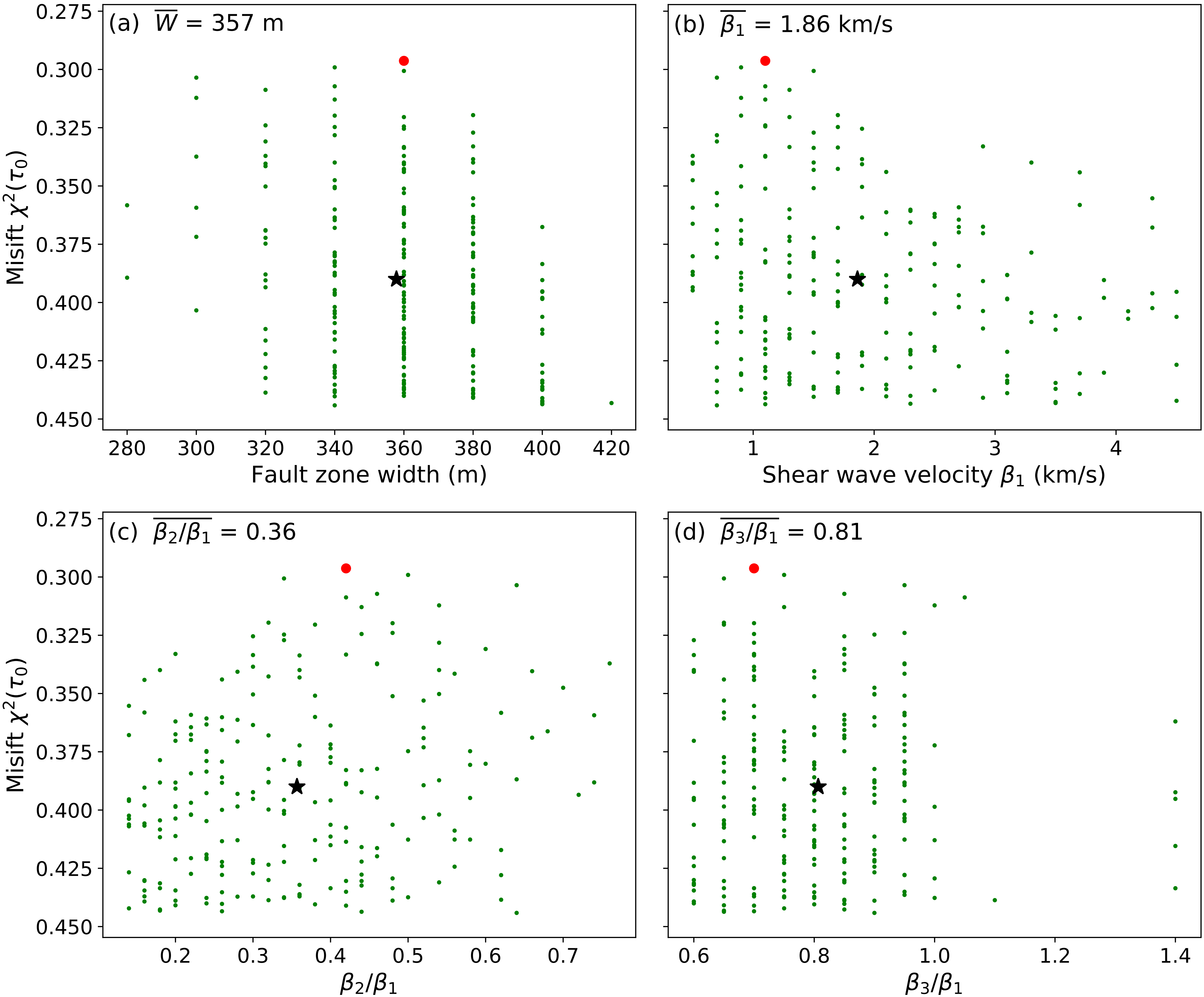

(a) $\overline{W}$ = 357 m
(b) $\overline{\beta_1}$ = 1.86 km/s
(c) $\overline{\beta_2/\beta_1}$ = 0.36
(d) $\overline{\beta_3/\beta_1}$ = 0.81
Misift $\chi^2(\tau_0)$
Fault zone width (m)
Shear wave velocity β_1 (km/s)
β_2/β_1
β_3/β_1
0.275
0.300
0.325
0.350
0.375
0.400
0.425
0.450
280
300
320
340
360
380
400
420
1
2
3
4
0.2
0.3
0.4
0.5
0.6
0.7
0.6
0.8
1.0
1.2
1.4